

# Curved Nanographenes: Multiple Emission, Thermally Activated Delayed Fluorescence, and Non-Radiative Decay

Sergio Ramírez-Barroso, Fernando Romeo-Gella, Jesús M. Fernández-García, Siyang Feng, Lara Martínez-Fernández, David García-Fresnadillo,\* Inés Corral,\* Nazario Martín,\* and Reinhold Wannemacher\*


The intriguing and rich photophysical properties of three curved nanographenes (CNG 6, 7, and 8) are investigated by time-resolved and temperature-dependent photoluminescence (PL) spectroscopy. CNG 7 and 8 exhibit dual fluorescence, as well as dual phosphorescence at low temperature in the main PL bands. In addition, hot bands are detected in fluorescence as well as phosphorescence, and, in the narrow temperature range of 100–140 K, thermally activated delayed fluorescence (TADF) with lifetimes on the millisecond time-scale is observed. These findings are rationalized by quantum-chemical simulations, which predict a single minimum of the  $S_1$  potential of CNG 6, but two  $S_1$  minima for CNG 7 and CNG 8, with considerable geometric reorganization between them, in agreement with the experimental findings. Additionally, a higher-lying  $S_2$  minimum close to  $S_1$  is optimized for the three CNG, from where emission is also possible due to thermal activation and, hence, non-Kasha behavior. The presence of higher-lying dark triplet states close to the  $S_1$  minima provides mechanistic evidence for the TADF phenomena observed. Non-radiative decay of the  $T_1$  state appears to be thermally activated with activation energies of roughly 100 meV and leads to disappearance of phosphorescence and TADF at  $T > 140$  K.

## 1. Introduction

Synthesis and characterization of molecular nanographenes (NGs), with or without heteroatoms, have been intensively pursued in recent years in view of their wide range of applications, such as the development of self-assembled nanomaterials or in fields like photocatalysis, energy conversion and storage, optoelectronics, single-molecule electronics, spintronics and magnetoelectronics, molecular switches and sensors or in multi-photon processes, nonlinear optics and bioimaging.<sup>[1]</sup> The structural features of molecular NGs include hydrogen-terminated or edge-functionalized polycyclic aromatic hydrocarbons;<sup>[2]</sup> heteroatom-doped NGs having heterocyclic motifs;<sup>[1b,d,e,h]</sup> or topologically complex curved nanographenes (CNGs) containing helicene moieties plus combinations of eight-, seven- and/or five-membered rings into the hexagonal

S. Ramírez-Barroso, J. M. Fernández-García, D. García-Fresnadillo, N. Martín  
Department of Organic Chemistry  
Faculty of Chemical Sciences  
Complutense University of Madrid  
Avenida Complutense s/n, Madrid 28040, Spain  
E-mail: dgfresna@ucm.es; nazmar@ucm.es  
S. Ramírez-Barroso, S. Feng, N. Martín, R. Wannemacher  
Imdea Nanoscience  
C/ Faraday 9, Cantoblanco, Madrid 28049, Spain  
E-mail: reinhold.wannemacher@imdea.org

F. Romeo-Gella, L. Martínez-Fernández, I. Corral  
Department of Chemistry  
Universidad Autónoma de Madrid  
Madrid 28049, Spain  
E-mail: ines.corral@uam.es  
L. Martínez-Fernández, I. Corral  
Institute for Advanced Research in Chemical Sciences (IAdChem)  
Universidad Autónoma de Madrid  
Madrid 28049, Spain

 The ORCID identification number(s) for the author(s) of this article can be found under <https://doi.org/10.1002/adma.202212064>

© 2023 The Authors. Advanced Materials published by Wiley-VCH GmbH. This is an open access article under the terms of the Creative Commons Attribution-NonCommercial License, which permits use, distribution and reproduction in any medium, provided the original work is properly cited and is not used for commercial purposes.

DOI: 10.1002/adma.202212064

carbon lattice of graphene.<sup>[3]</sup> Compared to graphene, whose overlapping conduction and valence bands pose limits to the development of some applications, NGs exhibit a non-zero energy gap, thus broadening the scope of potential uses.

The chemical induction of well-defined curvatures in molecular NGs (often with inherent chirality) leading to curved nanographenes (CNG), as well as steric interactions, may allow the fine tuning of their excited-state energy levels and, therefore, of their photophysical properties. In fact, this can be a promising strategy to obtain organic materials with interesting features related to appropriate relative energy differences and distributions of the singlet and triplet excited states manifolds. Examples of appealing unimolecular photophysical properties of organic materials would be dual fluorescence, phosphorescence, and thermally activated delayed fluorescence (TADF).<sup>[4]</sup> Furthermore, the peculiar topology and hydrophobicity of CNGs may allow bimolecular pathways based on interactions with other molecular entities or surfaces, giving rise to energy or electron transfer photochemical processes (e.g., Förster resonance, type II or type I photosensitization, etc.) that may advantageously broaden the field of application of CNGs.<sup>[5]</sup> All these distinctive emissions or excited-state reaction paths are susceptible to application in diverse areas such as quenching-based sensing of chemical species, data encryption, 3D printing, as emitters in organic light-emitting diodes (OLEDs), or in theranostics combining bioimaging (avoiding interference by the autofluorescence of biological samples) and photosensitization properties of reactive oxygen species (in photodynamic therapy treatments).<sup>[6]</sup> In particular, unimolecular deactivation pathways resulting in phosphorescence and TADF, when combined with chirality, are amenable for the smart development of high performance optoelectronic applications like data storage, security tags, chirality sensing, and next-generation displays.<sup>[7]</sup>

Phosphorescence is generated through two spin-forbidden processes, the non-radiative  $S_1 \rightarrow T_1$ , or, more generally,  $S_1 \rightarrow T_n$  intersystem crossing (ISC) and the radiative  $T_1 \rightarrow S_0$  transition. Therefore, for a purely organic molecule, the rate constant of intersystem crossing ( $k_{ISC}$ ) from a singlet excited state to a triplet excited state is typically small and the quantum yield of the intersystem crossing ( $\Phi_{ISC}$ ) is low, such that the population of triplet excited states is not favored. However, even if the triplet excited state is significantly populated, competition of the generally very slow radiative decay of the triplet state (rate constant  $k_{rT}$ ) with non-radiative deactivation ( $k_{nrT}$ ) and quenching processes ( $k_{qT}$ ) makes it a very challenging task to obtain organic materials with significant phosphorescence quantum yields ( $\Phi_p$ ) at room temperature. Several strategies have been developed to improve the quantum yields of ISC and of organic phosphorescence. ISC can be strongly enhanced, if the energy gap between the  $S_1$  and a  $T_n$  state is small and the  $S_1$  and  $T_n$  wave functions are nearly orthogonal.<sup>[8]</sup> Such near orthogonality can be achieved via  ${}^{3,1}(n\pi^*) \leftrightarrow {}^{1,3}(\pi\pi^*)$  transitions, for example in the case of molecules containing aldehyde or ketone functional groups,<sup>[9]</sup> or via transitions between charge-transfer (CT) and localized  $\pi\pi^*$ -type states ( ${}^{3,1}(\pi\pi^*)_{CT} \leftrightarrow {}^{1,3}(\pi\pi^*)_{loc}$ ).<sup>[10]</sup> Alternatively, by introducing heavy atom functional groups such as bromine and iodine substituents into organic molecules, the heavy atom effect can enhance spin-orbit coupling (SOC), and thus facilitate the ISC process, promoting  $k_{rT}$  and improving  $\Phi_p$ .<sup>[11]</sup> Rigid crys-

talline and glassy environments, which restrict vibrational and rotational motions that can induce decay of the triplet excited states have been used to inhibit non-radiative deactivation pathways. These rigid environments thus typically improve  $\Phi_p$  of organic systems at room temperature. Moreover, modifying the molecular packing, or adding supramolecular interactions like inclusion complexation and hydrogen bonding can also contribute to suppress the molecular vibrations of the triplet excited states to increase  $\Phi_p$ .<sup>[12]</sup>

Upconversion from the lowest triplet to the lowest singlet excited states through reverse intersystem crossing (RISC) gives rise to TADF, provided the energy gap ( $\Delta E_{S-T}$ ) between both excited states is small enough, typically below 0.3 eV, such that thermal energy is sufficient to populate the singlet state. Therefore, reducing the energy gap between the lowest excited singlet state and its nearest triplet state is of major importance in the case of TADF. This has been generally achieved by synthesizing organic dyes containing suitable combinations of electron-donor (D) and electron-acceptor (A) moieties connected via different types of bridges, usually with high twists or non-conjugated connections to obtain reduced overlaps between the highest occupied molecular orbitals (HOMOs, ideally located in the donor part) and lowest unoccupied molecular orbitals (LUMOs, preferably located in the acceptor fragment). These molecular architectures<sup>[10b]</sup> thus result in small energy differences between the first singlet ( $S_1$ ) and triplet ( $T_1$ ) excited states and therefore permit efficient RISC. In these molecules, intramolecular CT between D and A moieties is the dominant transition, leading to a lowest singlet state with CT character. Appropriately designed TADF dyes often rely on one of the following strategies: i) inducing a large steric hindrance in D–A molecular systems to produce a twisted intramolecular charge transfer (TICT) state; ii) allowing a through-space charge transfer (TSCT) with non-conjugated linkers by controlling the distance between the D and A units and also their relative orientation; or iii) taking advantage of multiple resonance effects in heteroaromatic compounds (e.g., with trisubstituted  $sp^2$  heteroatoms, such as boron or nitrogen with  $\pi$ -conjugated connections to either  $\pi$ -donor or  $\pi$ -acceptor groups). Moreover, the so-designed dyes display restricted rotation and increase the molecular rigidity, which suppresses the non-radiative deactivation and can also help to avoid severe aggregation potentially causing efficient excited state deactivation.<sup>[13]</sup> Similar to the enhancement of the case of ISC, the presence of high-lying triplet states ( $T_n$ ) can also help to promote TADF, which can be enhanced by taking advantage of near-resonant RISC from a thermally activated high-lying triplet state (hRISC) where energy up-conversion from a higher triplet state ( $T_n$ ,  $n \geq 2$ ) to the  $S_1$  state occurs.<sup>[14]</sup>

Furthermore, it has to be noted that chiral dyes exhibiting TADF properties combined with circularly polarized (CP) luminescence can show great potential in empowered OLED systems applied to high quality 3D, augmented-reality, and virtual reality displays.<sup>[15]</sup> In principle, CP-TADF systems would only require the addition of a chiral moiety (either a stereocentre, a chiral axis, or a planar chirality element) to the TADF dye. However, the development of efficient CP-TADF dyes is a challenging issue since several problems beyond their complex synthesis can occur, such as a low luminescence dissymmetry factor ( $g_{lum}$ ) value if the chiral moiety is not directly involved in the frontier

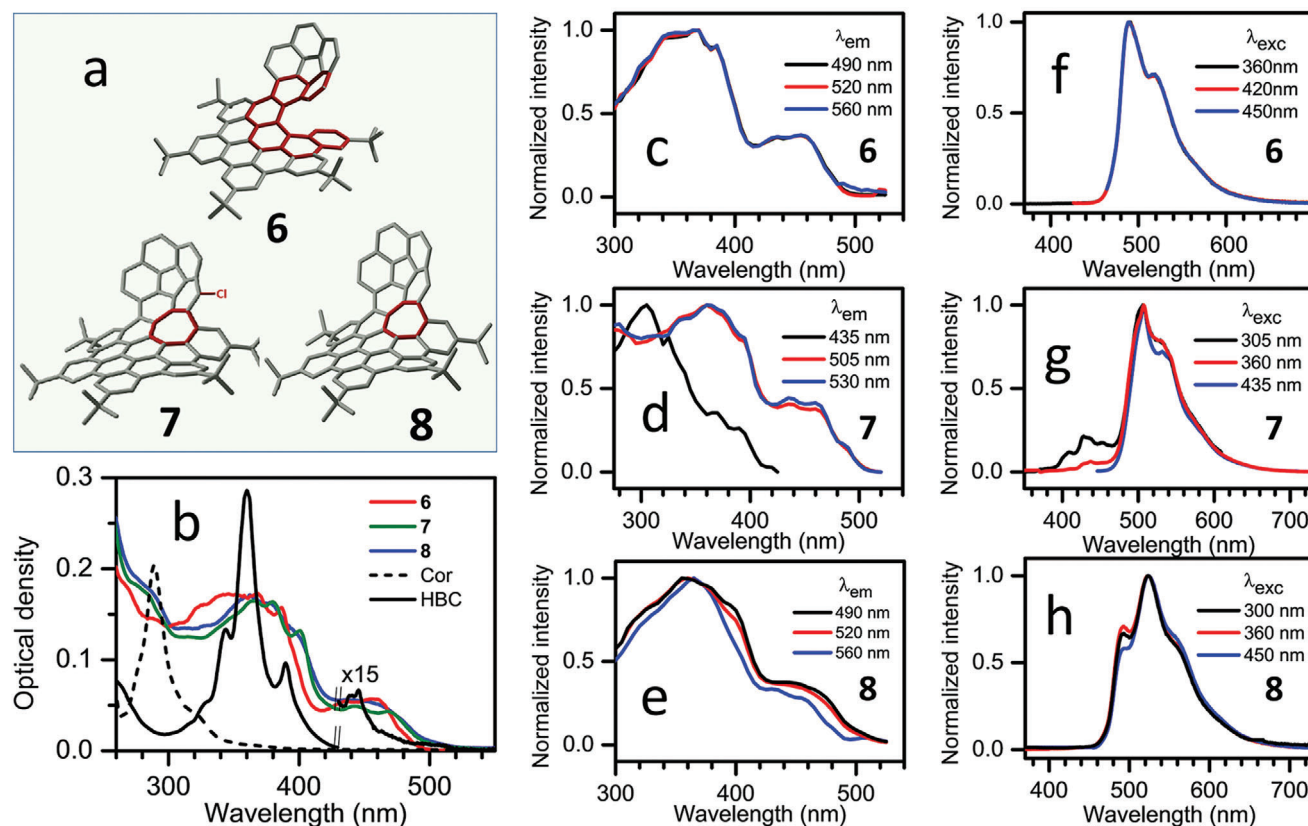


**Figure 1.** a) Curved nanographenes (CNG) **6**, **7**, and **8** (only one enantiomer shown). The loose [6]helicene of **6**, the chlorine atom of **7** and the cycloheptatrienically-constrained [6]helicene of **7** and **8** (due to the presence of the seven-membered ring) are highlighted in red. b) Absorption spectra in chloroform at room temperature of CNG **6** (red), **7** (blue) and **8** (green) and of their structural precursors **Cor** (black dash) and **HBC-tBu** (black). The visible portion of the **HBC-tBu** absorption spectrum ( $\geq 430$  nm) has been magnified ( $\times 15$ ). c–e) excitation spectra at the given detection wavelengths and f–h) photoluminescence spectra of **6**, **7**, and **8**, respectively, at the given excitation wavelengths.

molecular orbitals responsible for the lowest-lying electronic transition. Moreover, although a reduced HOMO–LUMO overlap is required for low  $\Delta E_{S-T}$  values and efficient TADF (usually at the expense of sacrificing color purity), large HOMO–LUMO overlaps would, in contrast, improve  $g_{lum}$  values by increasing the angle between the electric transition dipole moment and the magnetic transition dipole moment.<sup>[7,16]</sup>

Herein we report on the unusual photophysics of three different curved nanographenes (CNG **6**, **7**, and **8**) (Figure 1a; Figure S1, Supporting Information).<sup>[17]</sup> The studied CNG are composed of a corannulene (**Cor**) fragment of positive curvature and a modified hexabenzocoronene fragment (**HBC-tBu**) that can impart negative curvature via a seven-membered ring connection between the terminal rings of a [6]helicene. Depending on the type of attachment between both fragments, by forming either a loose-helicene (CNG **6**), a cycloheptatrienically constrained helicene (CNG **8**) or a cycloheptatrienically and sterically constrained helicene (CNG **7**), distinct and valuable photophysical properties can be observed. It must be mentioned that CNG **6** is inherently chiral and it has been synthesized as a racemic mixture.<sup>[17,18]</sup> To provide evidence for the purity of the samples used, in addition to the data presented in ref. [17], we are including in the SI high-resolution mass spectra, the high-resolution H-NMR and also the HPLC chromatograms for the three reported

compounds **6**, **7**, and **8** (Figures S32–S40, Supporting Information).

## 2. Results and Discussion

### 2.1. Photophysical Properties

#### 2.1.1. Absorption, Fluorescence Excitation and PL Spectra at Room Temperature

The UV–vis absorption spectra of CNG **6**, **7**, and **8**, and of their structural precursors **Cor** and **HBC-tBu** in  $\text{CHCl}_3$  are shown in Figure 1b and Table 1 collects the corresponding spectral data. The absorption spectra of the CNG are obviously much broader than the very narrow absorption of **Cor** and the absorption of **HBC-tBu**. In addition, the CNGs have a relatively intense absorption band in the blue part of the visible region. This is caused by the extension of the conjugation between both fragments of the CNG. The absorption maxima of the fragments, on the other hand, coincide quite well with maxima or shoulders of the CNG absorption spectra. Furthermore, the presence of a cycloheptatrienic connection within the [6]helicene moiety causes a redshift of  $\approx 20$  nm of the visible absorption band when comparing CNG

**Table 1.** Spectral data of the investigated compounds and of their structural precursors at room temperature.

CNG	$\lambda_{\text{abs}}^{\text{max}}$ [nm] <sup>a)</sup>	$\epsilon$ [ $10^3 \text{ mol}^{-1} \text{ dm}^3 \text{ cm}^{-1}$ ]	$\lambda_{\text{fluor}}^{\text{max}}$ [nm] <sup>b)</sup> (FWHM [eV], [nm])
Cor	289, 318 sh	31, 6.6	<b>420</b> , 440 <sup>c)</sup>
HBC-tBu	344, 360, 390, 445	64, 142, 46, 1.8	474, <b>483</b> , 492, 517 <sup>d)</sup>
<b>6</b>	346, 367, 386, 436, 456	73, 72, 65, 21, 22	<b>490</b> , 519 (0.30, 62)
<b>7</b>	367, 380, 401, 443, 467	77, 76, 62, 23, 20	430, <b>507</b> , 530 (0.25, 56)
<b>8</b>	362, 378, 441	68, 64, 20	493, <b>523</b> , 557 sh (0.32, 75)

<sup>a)</sup> Absorption peaks and shoulders (sh) in chloroform; <sup>b)</sup> Emission peaks in chloroform with the fluorescence maxima highlighted in bold numbers; <sup>c)</sup> In dichloromethane;<sup>[19]</sup> <sup>d)</sup> In tetrahydrofuran.<sup>[20]</sup>

**7** and **8** with CNG **6**, which may be of interest in view of potential optoelectronic applications requiring excitation by visible light.

Photoluminescence (PL) and PL excitation spectra of the CNGs, compare Figure 1f–h and Figure 1c–e, respectively, exhibit significant differences between the individual CNGs. Whereas the shape of the main emission band is similar for **6** and **7**, there is a redshift of the PL maximum of 17 nm from **6** to **7** and, in addition, a weak emission can be observed in the wavelength range  $\approx 390$ –470 nm in the case of **7**. The fluorescence excitation and emission spectra of the CNGs have been double checked with samples prepared in different years and, in the case of CNG **7**, an ultrapure sample has been examined with two different spectrofluorometers. We have found that the shape of this weak emission is strongly dependent on the concentration and the temperature of the sample (Figure S2, Supporting Information). This experimental finding can be accounted for by the well-known trend of  $\pi$ -extended molecular nanographenes to aggregate, typically stemming from  $\pi$ – $\pi$  and C–H $\cdots\pi$  supramolecular interactions.<sup>[3b,e,f]</sup> In the case of CNG **7** such aggregation is observed even in the micromolar concentration range and in a temperature interval close to room temperature (15–35 °C), thus affecting the relative fluorescence intensity and peak ratios depending on the variable aggregate/monomer proportion. This additional emission band exhibits a different excitation spectrum (black curve in Figure 1d), different also from the main band of the absorption spectrum. CNG **8**, on the other hand, exhibits a PL spectrum different from the ones of **6** and **7**, with shoulders on either side of the main PL maximum. PL maxima from the spectra acquired with excitation at the absorption maximum in the visible are gathered in Table 1. Excitation-emission maps (Figure S3, Supporting Information) exhibit no significant shift with the excitation wavelength and therefore demonstrate that the PL is essentially homogeneously broadened (compare Figure S3d–f, Supporting Information) at room temperature, except for slight variations in the spectra of **7** and **8** and for the additional high-energy emission of **7**, more easily recognizable on a logarithmic color scale (Figure S3h, Supporting Information).

### 2.1.2. Fluorescence Quantum Yields and Emission Lifetimes at Room Temperature

The fluorescence quantum yields and emission lifetimes in the ns range of the CNG at room temperature are collected in Table 2 and Table S1 (Supporting Information). The emission quantum yields of CNG **6** and **8** were determined by excitation at their

**Table 2.** Fluorescence quantum yield, fluorescence lifetimes, radiative and non-radiative deactivation rate constants of the singlet excited state, and upper limit of the intersystem crossing quantum yield of the investigated compounds in chloroform at room temperature under inert atmosphere unless otherwise indicated.  $\langle\tau_{\text{fluor},0}\rangle_{\text{int}}$ ,  $\langle\tau_{\text{fluor},\text{air}}\rangle_{\text{int}}$  intensity-weighted average decay times in purged and unpurged solutions, respectively.

CNG	$\Phi_{\text{fluor}}$	$\langle\tau_{\text{fluor},0}\rangle_{\text{int}}$ [ns] <sup>a)</sup>	$\langle\tau_{\text{fluor},\text{air}}\rangle_{\text{int}}$ [ns] <sup>a)</sup>	$k_r$ [ $\text{s}^{-1}$ ] <sup>b)</sup>	$k_{\text{nr}}$ [ $\text{s}^{-1}$ ] <sup>c)</sup>	$\Phi_{\text{ISC}}^{\text{d)}$
<b>6</b>	0.50	11.2	8.9	$4.5 \times 10^7$	$4.5 \times 10^7$	0.50
<b>7</b>	0.17, <sup>e)</sup> 0.21 <sup>f)</sup>	11.6	8.3	$1.5 \times 10^7$	$7.2 \times 10^7$	0.83
<b>8</b>	0.25	5.3	4.8	$4.7 \times 10^7$	$1.4 \times 10^8$	0.75

<sup>a)</sup> Intensity-weighted average lifetime, determined at the wavelength of the emission maximum;  $\langle\tau\rangle_{\text{int}} = \sum [I_i \tau_i^2] / \sum [I_i \tau_i]$ , where  $I_i$  and  $\tau_i$  are the individual pre-exponential factors and lifetimes of the multiexponential fit, respectively; <sup>b)</sup> Radiative deactivation rate constant from  $S_1$  to  $S_0$ , calculated from  $\Phi_{\text{fluor}} / \langle\tau_{\text{fluor},0}\rangle_{\text{int}}$ ; <sup>c)</sup> Upper limit of the non-radiative deactivation rate constant from  $S_1$ , calculated from  $(1 - \Phi_{\text{fluor}}) / \langle\tau_{\text{fluor},0}\rangle_{\text{int}}$ ; <sup>d)</sup> Upper limit of the intersystem crossing quantum yield, calculated from  $1 - \Phi_{\text{fluor}}$ ; <sup>e)</sup> Excitation at 470 nm; <sup>f)</sup> Excitation at 305 nm. Values of  $k_r$ ,  $k_{\text{nr}}$ , and the upper limit of  $\Phi_{\text{ISC}}$  are calculated neglecting any potential reverse intersystem crossing at room temperature as well as intermolecular interactions.

absorption maxima and are in excellent agreement with previously reported data.<sup>[17]</sup> On the other hand, due to its additional emission at short excitation wavelengths and the associated variability of its excitation spectrum (Figure 1; Figures S2 and S3, Supporting Information), CNG **7** shows  $\Phi_{\text{fluor}} = 0.17$  when excited above 400 nm but values increasing to 0.21 when excited at 305 nm. Regarding the PL lifetimes of the CNG, all the molecular nanographenes under study present multiexponential decays at room temperature, and no dependence on concentration has been found in the tested  $10^{-7}$  to  $10^{-5}$  M concentration range; however, slightly dissimilar behaviors are shown when comparing the PL decays of CNG **6** on the one hand and CNG **7** and **8** on the other hand (Table S1, Supporting Information). CNG **6** requires bi-exponential fits and, irrespective of the selected detection wavelength (emission peak or shoulder), the PL decays are fitted to the same individual lifetimes, within experimental uncertainty, resulting in the same average lifetimes. However, CNG **7** and **8** not only require bi-exponential or tri-exponential functions to fit the experimental decays, respectively, but both of them show different decay fitting parameters depending on the selected detection wavelength (emission peak, shoulder or tail), hinting at a complex nature of the electronic singlet states and their potential energy surfaces from where emission takes place (see the discussion below), consistent with the variations in the fluorescence excitation and emission spectra of these two CNGs



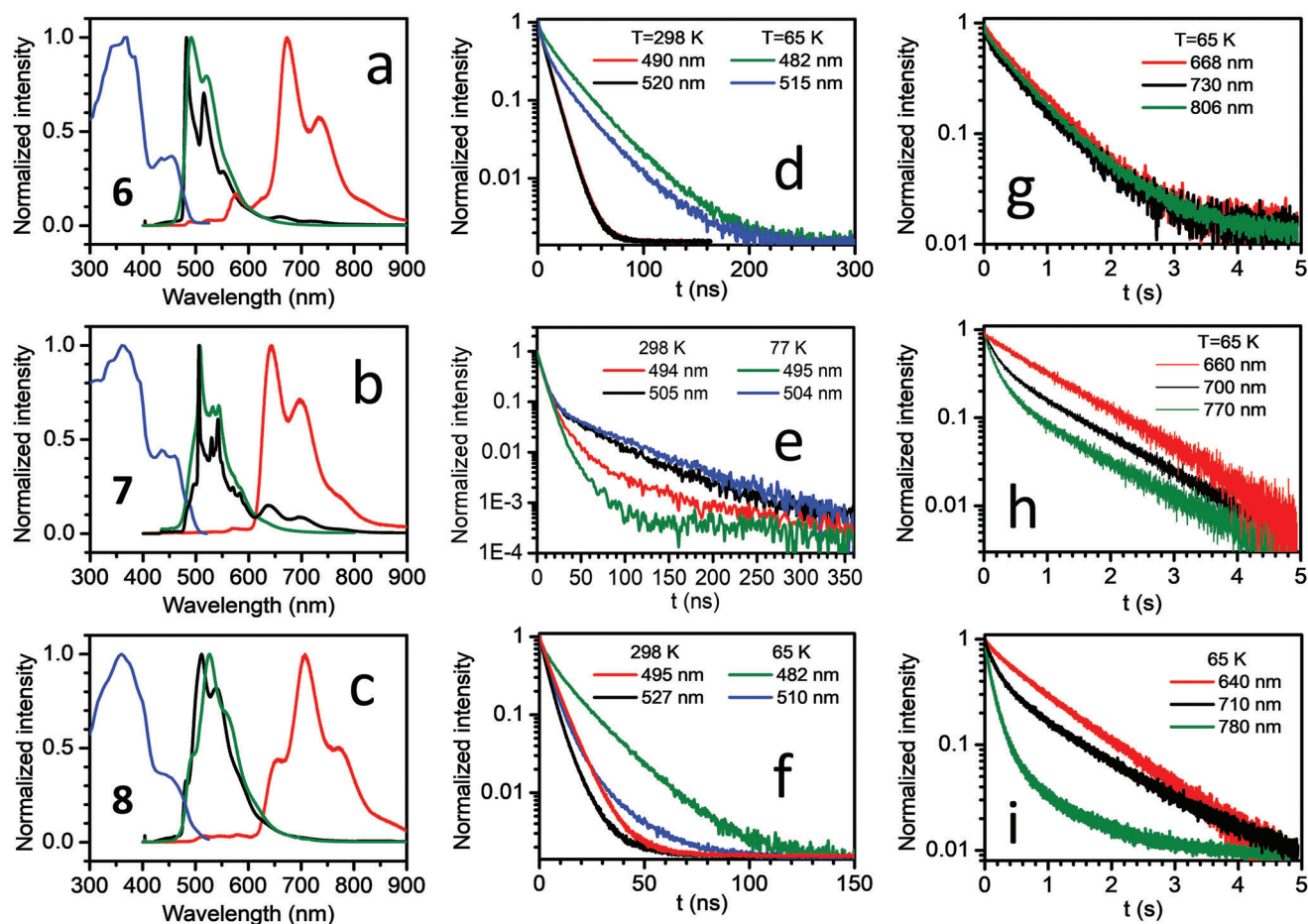


**Figure 2.** a–c) PL excitation spectra with detection at the wavelength of the PL maximum (blue), PL spectra at room temperature (green) and at  $T = 65$  K (black), as well as gated spectra acquired at  $T = 65$  K (red); d–f) fluorescence decays; and g–i) phosphorescence decays at the indicated wavelengths of **6** (a,d,g), **7** (b,e,h), and **8** (c,f,i) in *n*-octane.  $\lambda_{\text{exc}} = 405$  nm.

(Figure 1). Finally, the radiative ( $k_r$ ) and overall non-radiative ( $k_{nr}$ ) deactivation rate constants of  $S_1$  were estimated from the values of the fluorescence quantum yield and mean emission lifetimes, as detailed in Table 2. We also report there the upper limit of the intersystem crossing quantum yield ( $\Phi_{\text{ISC}}$ ) of the CNG, neglecting here any potential reverse intersystem crossing, or intermolecular interactions and assuming for the present purpose that  $S_1$  is the only singlet state populated at room temperature. It should finally be noted that long-lived PL with lifetimes significantly longer than those of the fluorescence, which would be due to phosphorescence or TADF, was not observed in any of the CNGs at room temperature even after purging.

### 2.1.3. Fluorescence, Phosphorescence and Thermally Activated Fluorescence at Low Temperature

**Figure 2a–c** shows the normalized PL spectra of CNGs **6**, **7**, and **8**, respectively, in *n*-octane at room temperature (green lines) and at  $T = 65$  K (black lines) under continuous wave (cw) excitation, as well as phosphorescence spectra (red lines), acquired by elec-

**Table 3.** Fluorescence and phosphorescence spectral maxima and PL lifetimes of the investigated compounds and of their structural precursors in *n*-octane at 65 K.

CNG	$\lambda_{\text{fluo}}^{\text{max}} / E_{\text{fluo}}^{\text{max}}$ [nm (eV)]	$\langle \tau_{\text{fluo}} \rangle_{\text{int}}$ [ns]	$\lambda_{\text{phos}}^{\text{max}} / E_{\text{phos}}^{\text{max}}$ [nm (eV)]	$\langle \tau_{\text{phos}} \rangle_{\text{int}}$ [s]
<b>6</b>	483 (2.57)	26.5	673 (1.84)	0.67
<b>7</b>	506 (2.45)	30.0	640 (1.94)	1.0
<b>8</b>	511 (2.42)	6.7	707 (1.75)	0.9
<b>Cor</b>	437 (2.84)	11.4	600 (2.07)	0.16
<b>HBC-tBu</b>	482 (2.57)	53.1	573 (2.16)	1.0

tronic gating after pulsed excitation. **Table 3** and Table S2 (Supporting Information) list the positions of the spectral maxima and shoulders. For the investigation of the temperature dependence of the PL, the solvent *n*-octane was chosen in view of additional experiments performed at lower temperature, which are not to be discussed here. As shown in Figure S4 (Supporting Information) for the case of CNG **7**, both solvents,  $\text{CHCl}_3$  and

n-octane, result in very similar fluorescence and phosphorescence spectra. The spectra acquired at 65 K generally exhibit some blue shift of the PL maxima compared to the room temperature spectra due to the rigidification of the matrix and the refractive index change upon freezing. Significant spectral narrowing indicates reduced thermal broadening.

To investigate the high-energy PL of **7** in the range  $\approx 380$ – $470$  nm (see Figure 1g) in more detail, temperature-dependent PL spectra were acquired with quasi-cw excitation at 355 nm at 1 kHz repetition rate (Figure S5a, Supporting Information). The high-energy PL obviously has maximum intensity at  $\approx 230$  K relative to the main PL band and then diminishes as the temperature is lowered, although it is still visible at 77 K. This suggests the identification of this band as a hot band due to PL from a higher singlet ( $S_n$ ) state. The increase in intensity when the temperature changes from 300 to 230 K should then be due to reduced non-radiative decay (internal conversion, IC) and its decrease from 230 to 77 K due to reduced thermal occupation. The presence of this band even at 77 K suggests that  $S_n$  can be populated from higher singlets as well as thermally populated from  $S_1$ . PL from a higher singlet at low temperatures, where it cannot be thermally populated, simultaneously signifies reduced rates of IC. From the onsets of the high-energy and main fluorescence bands at  $\approx 370$  nm (3.35 eV) and  $\approx 470$  nm (2.64 eV), respectively, an  $S_n$ – $S_1$  gap for CNG **7** of  $\approx 0.7$  eV can be deduced in this case. This appears to be too high for thermal population directly from  $S_1$ . However, the possible presence of other singlets within this energy range with populations trapped within them due to barriers in the electronic potential energy surface could explain the observations. On the other hand, the PL decays in this high energy band are longer than those of the main PL band, as shown in Figure S5b (Supporting Information), contrary to expectations. This detail will be discussed below in the context of the quantum-chemical calculations.

The PL spectra acquired under continuous wave (cw) excitation, dominated by fluorescence, and the phosphorescence spectra are overall quite like each other in structure and width, as becomes more appreciable when plotting them as a function of photon energy (Figure S6, Supporting Information). This indicates very similar vibronic coupling and, hence, the same orbital character of both,  $S_1$  and  $T_1$ . As an exception from this similarity, the fluorescence of **7**, however, is much more structured than the one of **6** or **8**, which is probably due to the steric hindrance caused by the chlorine atom and the associated stiffening of the molecule. Interestingly, there also appears a higher energy band of the phosphorescence, located at  $\approx 570$  nm, which is especially notable in the case of **6**. This band will be discussed again below.

The fluorescence decays of **6**, **7**, and **8** at 65 K (or 77 K, respectively) are shown in Figure 2d–f, respectively, and the phosphorescence decays in Figure 2g–i, respectively, for various wavelengths. Corresponding fit parameters are listed in Table 3 and Tables S3 and S4 (Supporting Information). The fluorescence decay times are relatively long, especially for **6** and **7**, implying small transition dipole moments. This is already the case for the structural precursors **Cor** and **HBC-*t*Bu** of the CNGs (compare Table 3 and Figure S7, Supporting Information). The phosphorescence decays on a time scale of seconds in all cases, pointing to extremely small radiative rates for the spin-forbidden transitions. Phosphorescence is also observed for the structural precursors,

again with lifetimes on the scale of seconds, although **Cor** shows the shortest phosphorescence decay among the CNGs and their precursors. In the case of **6** and in the case of the fragments **Cor** and **HBC-*t*Bu**, the decays at room temperature are independent of the wavelength and a small wavelength dependence at 65 K can be attributed to a weak background signal. In the case of **7** and **8**, on the other hand, the fluorescence as well as the phosphorescence decays are strongly wavelength-dependent, providing evidence for the existence of more than one emitting state. The near biexponential character of the decays (compare Tables S3 and S4, Supporting Information) points to dual fluorescence and dual phosphorescence of the CNG. The structural precursors, on the other hand, exhibit essentially wavelength-independent decays (Figure S7, Supporting Information) and small variations are probably again due to some weak background signals, implying that the dual character of fluorescence and phosphorescence is an intrinsic property of the CNG.

Another interesting observation relates to Figure S7 (Supporting Information): whereas the fluorescence of **Cor** shifts only very little with the excitation wavelength, less than 30 meV, the phosphorescence experiences a very large shift of  $\approx 0.3$  eV comparing excitation at 405 and 300 nm, respectively (Figure S7a,d, Supporting Information). Nevertheless, the shape of the spectra is very similar, although less resolved in the case of  $\lambda_{\text{exc}} = 405$  nm. The reason for this effect is currently unclear, because it implies a large change in singlet-triplet splitting, which is determined by the exchange interaction. It should be noted, however, that exciting at 405 nm is equivalent to excite very far in the low energy wing of the absorption band, which could correspond to molecules distorted by the solid matrix. In this context it may be of interest to note that the bowl-to-bowl inversion barrier for (ethyl)corannulene was previously determined to be only 0.50 eV from the ground bowl state to the transition planar form.<sup>[21]</sup> It may be that in such environments mechanical stress is sufficient to planarize or invert the bowl of corannulene. Further quantum-chemical calculations are required to clarify whether a change in curvature might cause a significant change in the singlet-triplet splitting of **Cor**.

Interestingly, the gated spectra exhibit significant variation at temperatures in the intermediate range between room temperature and 65 K. Figure 3a–c shows the gated spectra for **6**, **7**, and **8**, respectively, for the temperatures indicated in the figures. It is immediately clear from the figures that the phosphorescence is strongly quenched with increasing temperature. The quenching of absolute intensities is shown in Figure 3d,g for **6**, Figure 3e,h for **7**, and Figure 3f,i for **8** for two wavelengths in the phosphorescence band in each case. The absolute intensities exhibit a near Arrhenius behavior at higher temperatures with the activation energies indicated in the figures ranging from 77 to 175 meV. Those energies could correspond to activation of molecular vibrations. The spectra of Figure 3 normalized to the emission maxima (Figure S8, Supporting Information) evidence a complex behavior of the phosphorescence spectra particularly of **7**, consisting in non-monotonic shifts of the phosphorescence maxima with temperature and a significant change in relative intensities of the two main phosphorescence maxima. In addition, a high energy emission band is observed in the wavelength range  $\approx 500$ – $600$  nm, which peaks at certain temperatures before it disappears together with the phosphorescence.

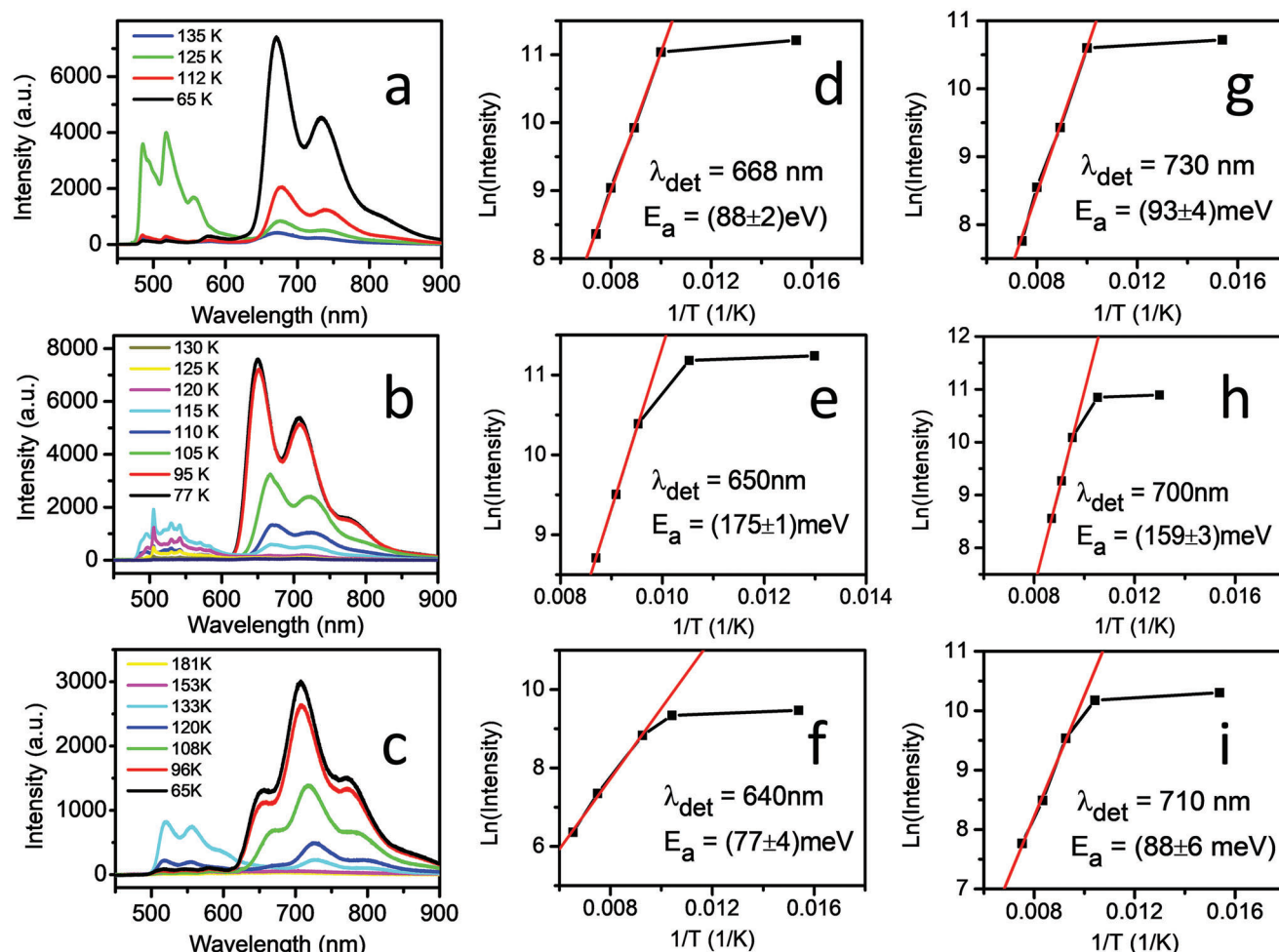


**Figure 3.** a–c) Gated emission spectra, at different temperatures, as indicated in the figures, and d–i) phosphorescence intensities at the given wavelengths as a function of temperature of **6** (a,d,g), **7** (b,e,h), and **8** (c,f,i), respectively. Activation energies derived from the Arrhenius plots are stated in the figures.

This high-energy emission band coincides with the fluorescence spectrum as can be recognized more easily in **Figure 4** and can therefore be identified as a TADF band. Whereas triplet–triplet annihilation (TTA) at first sight could offer an alternative explanation for the appearance of this band, it can be excluded, because TTA is inefficient in our samples, which are highly diluted in a solid, spectroscopically inactive host. This is the case, because molecular diffusion cannot occur in the solid and therefore only triplet exciton diffusion could possibly lead to TTA. Triplet exciton diffusion, on the other hand, can only be based on Förster resonant energy transfer (FRET) or Dexter energy transfer. Both have interaction ranges (FRET: typically, 1–5 nm, Dexter energy transfer: less than  $\approx 1$  nm) much smaller than the average intermolecular distance in our highly diluted samples (10  $\mu\text{m}$ , average intermolecular distance  $\approx 50$  nm). Moreover, triplet exciton diffusion by FRET can be excluded because of the extremely small transition dipole moments of the CNG between  $T_1$  and the ground state  $S_0$ , leading to radiative phosphorescent lifetimes in the range of seconds (these transition dipole matrix elements are required for FRET even though FRET is not a radiative process). In addition, thermal activation of the diffusion-limited bi-

molecular TTA reaction coefficient within a few degrees Kelvin can be excluded. The latter would be required to produce the observed non-monotonic temperature dependence and narrow temperature range of the delayed fluorescence. The disappearance of this band is, of course, determined by the time resolution of the gated spectra, where only photons that are emitted after a delay of 30 ms and within an integration time of 200 ms contribute (compare the Experimental section in the Supporting Information).

The thermally activated quenching of the phosphorescence intensities or thermally activated non-radiative decay rates should also be reflected in the phosphorescence lifetimes. Figure S9 (Supporting Information) shows the phosphorescence lifetimes in Arrhenius plots and evidently, the thermal dependence cannot be described as well by an Arrhenius behavior as it is the case for the absolute intensities. This is caused by the very small phosphorescence intensities at higher temperatures and the interference of possible weak background signals. Nevertheless, thermal activation energies derived from Figure S9 (Supporting Information) still coincide surprisingly well with those of Figure 3 for **6** and **8** and both deviate less than a factor of 1.6 for **7**. Interestingly,



**Table 4.** The onsets of fluorescence and phosphorescence spectra of the investigated compounds and of their structural precursors in n-octane at 65 K and singlet–triplet splitting as well as triplet–triplet splitting derived from them.

CNG/Fragment	$\lambda_{\text{onset}}^{\text{fluor}}/E_{\text{onset}}^{\text{fluor}}$ [nm (eV)]	$\lambda_{\text{onset}}^{\text{pho}}/E_{\text{onset}}^{\text{pho}}$ [nm (eV)]	$\Delta E_{S_1-T_1}$ [eV]	$\lambda_{\text{onset}}^{\text{pho,2}}/E_{\text{onset}}^{\text{pho,2}}$ [nm (eV)]	$\Delta E_{S_1-T_2}$ [eV]	$\Delta E_{T_{T1}-T_2}$ [eV]
<b>6</b>	471 (2.63)	639 (1.94)	0.69	560 (2.21)	0.42	0.27
<b>7</b>	473 (2.62)	612 (2.03)	0.59	574 (2.16)	0.46	0.13
<b>8</b>	471 (2.63)	617 (2.01)	0.62	564 (2.20)	0.43	0.19
<b>Cor</b> ( $\lambda_{\text{exc}} = 300$ nm)	373 (3.32)	475 (2.61)	0.71	–	–	–
<b>HBC-tBu</b>	460 (2.70)	563 (2.20)	0.50	–	–	–

Figure S8 (Supporting Information) shows that an emission band at  $\approx 570$  nm, marked by black arrows, appears also to be thermally activated although it is not present in the fluorescence spectrum. This allows the tentative identification of this band with a thermally excited  $T_2$  (or  $T_n$ ) state. The fact that this band is present already at low temperatures, e.g.,  $T = 65$  K suggests population trapping in  $T_2$  after pulsed excitation and, hence, retarded non-radiative relaxation of this state. It appears unlikely that the activation of TADF occurs from the lowest triplet  $T_1$ , which from the onsets of the phosphorescence spectra at 65 K can be placed at 1.94, 2.03 and 2.01 eV for **6**, **7**, and **8**, respectively, whereas the onsets of the fluorescence spectra indicate  $S_1$  positions at 2.63, 2.62 and 2.63 eV, respectively, resulting in singlet–triplet gaps  $\Delta E_{S_1-T_1}$  of 0.69, 0.59 and 0.62 eV, respectively (compare Table 4). For **Cor** and **HBC-tBu** the corresponding spectra at 65 K (compare Figure S7d,f, Supporting Information) result in values of the singlet–triplet splitting of 0.44 and 0.50 eV, respectively. Table 4 also lists the estimated onsets of the band at  $\approx 570$  nm and the corresponding  $S_1-T_2$  singlet–triplet gaps. From those estimated onsets the positions of  $T_2$  can be calculated resulting in  $S_1-T_2$  splitting of 0.42, 0.46 and 0.43 eV for **6**, **7**, and **8**, respectively. The decay of the TADF signals cannot be followed over the full temperature range because of vanishing amplitudes at low and high temperatures. As an example, however, Figure S10 (Supporting Information) demonstrates that the TADF signal of **6** observed at  $T = 135$  K and  $\lambda = 486$  nm decays with an intensity-averaged decay time of 25 ms, whereas the phosphorescence at the same tem-

perature and  $\lambda = 673$  nm decays with a significantly longer decay time, but on a similar scale, of 92 ms. In the standard case of TADF activated from  $T_1$ , in the whole temperature range equal decay times would be expected for the emission from  $T_1$  (here termed “phosphorescence”) and for the TADF from  $S_1$ , in addition to a fast decay in the nanosecond range.<sup>[14c,22]</sup> The fact that both decay times are observed to be unequal suggests that more than two electronic states ( $S_1/T_1$ ) are involved in the TADF, in line with the previous discussion. Unfortunately, due to the weakness of the emission at  $\approx 570$  nm, identified above with emission from  $T_2$ , and its overlap with TADF, the decay at this wavelength cannot be measured independently from that of the TADF signal.

The observation of TADF in the CNGs raises the question whether this effect can also be observed in their structural precursors. Figure S11 (Supporting Information) displays temperature-dependent gated spectra for **Cor** and **HBC-tBu**. **HBC-tBu** evidently does not exhibit TADF at the temperatures where the spectra were registered, whereas **Cor** indeed exhibits TADF, but at significantly higher temperatures than for the CNGs. In the case of **Cor**, a gap  $\Delta E_{S_1-T_1} = 0.71$  eV can be estimated from the high-energy onsets of the fluorescence and phosphorescence spectra of Figure S7d (Supporting Information), which, similar to the CNGs, is too large to allow direct thermal activation of  $S_1$  in the temperature range considered here. The conclusion is again that there must exist a higher triplet state  $T_n$  with a sufficiently long lifetime to allow thermal activation of  $S_1$ .

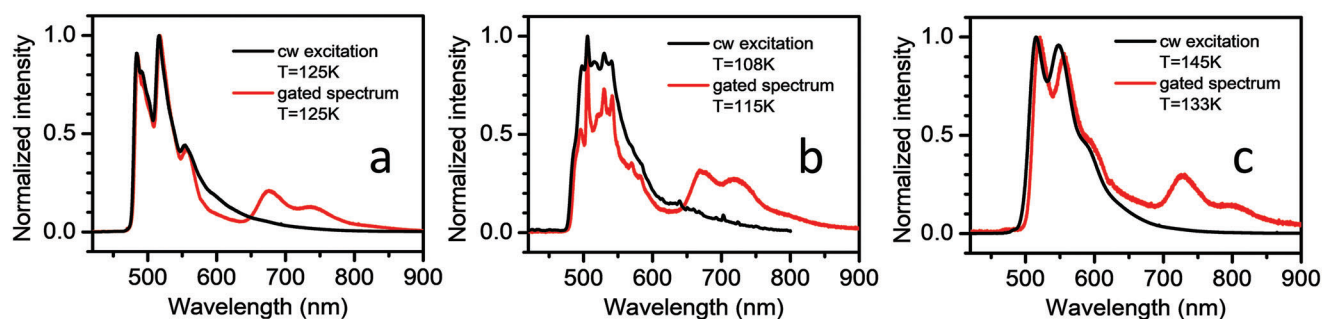


**Figure 4.** Comparison of fluorescence (black) spectra under continuous excitation at  $\lambda_{\text{exc}} = 405$  nm and gated spectra (red) in the spectral range (450–650) nm at the given temperatures for CNGs **6** (a), **7** (b), and **8** (c). Gated spectra in the given wavelength range agree well with the fluorescence spectra, which, together with their temperature dependence (compare with Figure 3 unequivocally identifies the corresponding emission as thermally activated delayed fluorescence (TADF)). The features in the gated spectra at longer wavelengths correspond to phosphorescence (compare with the red graphs in Figure 2). We have verified that the small temperature differences of the spectra appearing in (b,c) do not lead to any significant change in the shape of the spectra.



**Table 5.** Bimolecular quenching rate constants  $k_{qS}^{O_2}$  of the investigated compounds by molecular oxygen, proportion of singlet excited states quenched  $P_S^{O_2}$ , fraction of singlet excited states statically quenched  $f_{static}$ , singlet oxygen production quantum yield  $\Phi_\Delta$  and lower limit  $f_\Delta^T$  of the fraction of triplet states quenched by ground-state molecular oxygen leading to singlet oxygen production in chloroform at room temperature under inert atmosphere unless otherwise indicated.

CNG	$k_{qS}^{O_2}$ [mol <sup>-1</sup> dm <sup>3</sup> s <sup>-1</sup> ] <sup>a)</sup>	$k_{qS}^{O_2 \tau}$ [mol <sup>-1</sup> dm <sup>3</sup> s <sup>-1</sup> ] <sup>b)</sup>	$P_S^{O_2 c)}$	$P_S^{O_2 \tau d)}$	$f_{static}^e)$	$\Phi_\Delta^f)$	$f_\Delta^T g)$
6	$1.3 \times 10^{10}$	$9.6 \times 10^9$	0.29	0.21	0.10	0.36	0.61
7	$1.7 \times 10^{10}$	$1.4 \times 10^{10}$	0.32	0.28	-	0.47	0.53
8	$9.8 \times 10^9$	$8.1 \times 10^9$	0.095	0.094	-	0.40	0.51

a) Bimolecular quenching rate constants by  $O_2$  obtained after Stern–Volmer analysis from fluorescence intensity measurements; b) Bimolecular quenching rate constants by  $O_2$  obtained after Stern–Volmer analysis from fluorescence average lifetimes, where intensity weighted or amplitude weighted mean lifetimes give equivalent values, within experimental error; c) Probability of singlet excited state quenching by  $O_2$ , determined from fluorescence intensity measurements; d) Probability of singlet excited state quenching by  $O_2$ , determined from fluorescence average lifetimes; e) Fraction of singlet excited states statically quenched by molecular oxygen; f) Singlet oxygen production quantum yields; g) Fraction of triplet excited states quenched by molecular oxygen leading to singlet oxygen production.

#### 2.1.4. Excited States Quenching by Molecular Oxygen and Singlet Oxygen Production Quantum Yield

Steady-state and time-resolved experiments concerning the quenching by molecular oxygen allowed to gain insights on the transition of the CNGs from the singlet to the triplet excited state. The Stern–Volmer equation and the intensity-weighted average lifetimes ( $\langle \tau \rangle_{int}$ ) were used to calculate the quenching parameters since, overall, better agreement between intensity and lifetime results was obtained when  $\langle \tau \rangle_{int}$  was used, in particular, in the case of the quite complex CNG 7 system.<sup>[23]</sup> Quenching of the  $S_1$  excited state by molecular oxygen was evidenced by the changes in the mean lifetimes of the air-equilibrated solutions compared to the  $N_2$ -purged samples. Bimolecular quenching rate constants by  $O_2$  are diffusion-controlled as shown by the  $k_{qS}^{O_2}$  values  $\approx 10^{10}$  mol<sup>-1</sup> dm<sup>3</sup> s<sup>-1</sup> (Table 5) and the values determined from the intensities and those determined from the lifetimes essentially agree, as is the case for the probabilities of singlet excited state quenching by  $O_2$  ( $P_S^{O_2}$ ) in the case of CNG 7 and 8. However, a marked difference was surprisingly obtained for CNG 6, where  $P_S^{O_2 I} = 0.29$  from steady-state intensity measurements, but  $P_S^{O_2 \tau} = 0.21$  from time-resolved lifetime measurements (Table 5), which implies 10% static quenching ( $f_{static}$ ) by molecular oxygen in the case of CNG 6.

On the other hand, the CNGs can produce singlet oxygen,  $^1O_2(^1\Delta_g)$ , not only by quenching of their triplet excited states by ground-state molecular oxygen, but, due to its long-lived nature, after singlet excited state quenching by  $O_2$ , following the so-called  $O_2$ -induced enhanced intersystem crossing (EISC) process. Therefore, the CNGs may be classified as TC photosensitizers where quenching of  $S_1$  by  $O_2$  catalyzes the production of  $T_1$ . This apparently happens although singlet oxygen cannot be directly generated from  $S_1$  (because  $E_{S1} - E_{T1} < E_\Delta$ , being  $E_\Delta$  the energy difference between singlet oxygen and ground-state triplet oxygen, 0.97 eV) as can be deduced from the energy values collected in Table 4.<sup>[24]</sup> Singlet oxygen production quantum yields ( $\Phi_\Delta$ ) were determined by chemical scavenging of  $^1O_2$  with 1,3-diphenylisobenzofuran (Figures S12 and S13, Supporting Information). The obtained results are collected in Table 5 and are significantly lower than the upper limit of  $\Phi_{ISC}$ .

#### 2.1.5. Excited State Properties in the Solid State: Fluorescence Spectra, PL Decays and Quenching by Molecular Oxygen

Figure S14 (Supporting Information) shows the fluorescence spectra of the CNG powders and the PL decays under nitrogen and in air-equilibrated conditions. Table S5 (Supporting Information) collects the results of the tri-exponential analysis of the emission decays under nitrogen and for air-equilibrated samples. Negligible quenching by molecular oxygen has been observed in the solid state in the case of CNG 6, while weak deactivation is noted for CNG 8 ( $P_S^{O_2 \tau}$  0.09) that is equivalent to that observed in chloroform solution (Table 5); however, a surprisingly efficient quenching of the singlet excited state of CNG 7 has been observed ( $P_S^{O_2 \tau}$  0.75), that exceeds the values observed in solution ( $P_S^{O_2}$  0.32,  $P_S^{O_2 \tau}$  0.28).

### 2.2. Computational Studies

#### 2.2.1. Absorption Spectra

With the aim of interpreting the experimental absorption spectrum, for each derivative we have modelled the vibrationally-resolved electronic absorption spectrum at the wB97X-D/def2-SVP level of theory considering the system embedded in a chloroform continuum (Figure 5). We have limited our analysis to the 8 lowest excited states ( $S_1$ – $S_8$ ), which cover the energy range between 350 and 500 nm. The electronic absorption spectra considering the first 100 electronic states and covering the spectral range of wavelengths between 300–550 nm can be found in Figure S15 (Supporting Information).

Our simulations reveal that the  $S_1$  and  $S_2$  states, and especially the former, are the main contributors to the broad and weak low-energy absorption band. The  $S_1$  and  $S_2$  states in all three compounds are vertically degenerate and no ordering can be precisely assigned. The following and brighter absorption band with significant vibrational structure is the result of the combination of different excitations: a) for CNG 6, the main contributing excitations are  $S_4$ ,  $S_7$  and  $S_8$ ; b) for CNG 7,  $S_4$ ,  $S_6$  and  $S_8$ ; and c) for CNG 8,  $S_4$ ,  $S_5$ ,  $S_7$  and  $S_8$ . Nevertheless, all considered states contribute to the absorption spectra. No absolutely dark states were found in the range of wavelengths considered. As expected,

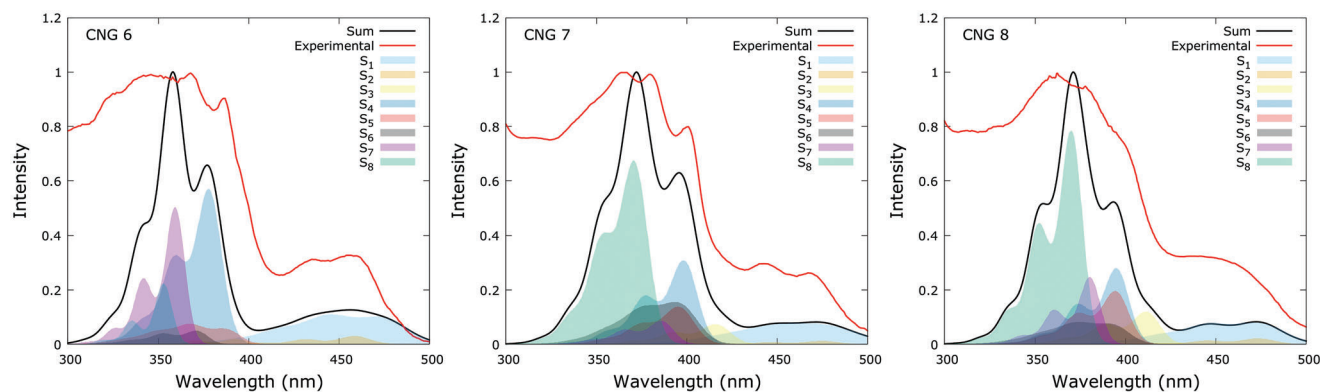


**Figure 5.** In black, calculated normalized vibrationally-resolved absorption spectra using a FWHM of 0.05 eV at room temperature of CNG **6** (left), **7** (center) and **8** (right) at the TD-wB97X-D/def2-SVP/PCM = (CHCl<sub>3</sub>) level of theory, superimposed to the experimental signal in red. The contribution of the different excited states to the absorption signal is denoted by the areas following the color code defined in the inset. The theoretical spectra were redshifted by 0.5, 0.6, and 0.6 eV, respectively, for a better comparison with experimental data.

all these states show a  $\pi\pi^*$  character. A detailed description of the character of these transitions has been obtained resorting to electron–hole correlation plots (Figures S16–S18, Supporting Information), where the electron density (de)localization along the two molecular moieties (**HBC-tBu** and **Cor**) composing the CNG was investigated for each of the excited states at the Franck–Condon (FC) geometry. It is relevant to highlight that, despite observing a certain degree of delocalization between both moieties, no significant CT character is detected, in line with the calculated oscillator strengths. A careful inspection of the electron–hole correlation plots reveals that the lower energy transitions ( $S_1$  and  $S_2$ ) are mainly localized on the **HBC-tBu** moiety, while intra-**Cor** excitations are frequently observed in higher energy transitions, in agreement with the experimental absorption spectra of the independent chromophores (Figure 1b). These findings hint at the little interplay existing between both molecular subunits.

The absorption spectra of the **Cor** and **HBC-tBu** fragments were obtained at the same level of theory as that employed for the CNGs and are shown in Figure S19 (Supporting Information) left panel. The agreement with the experimental absorption spectra was satisfactory, upon redshifting by 0.85 and 0.7 eV our theoretical excitation energies. It is interesting to remark that the lower-lying excitations have extremely low oscillator strengths (compare the discussion below in the context of the radiative rates) and the main absorption peaks are ascribed to higher-lying excited states:  $S_6$ – $S_8$  for **Cor** and  $S_5$ – $S_6$  for **HBC-tBu**. Despite the excellent vibronic correspondence between theory and experiment at the higher-energy edge of the absorption peak, the longer wavelength range of the band is not well reproduced.

### 2.2.2. Singlet Potential Energy Surface and Fluorescence

To provide molecular insight into the photophysical properties recorded for these systems, we have extensively explored the potential energy surface (PES) away from the FC region by undertaking geometry optimizations for the first 8 excited states and looking for interstate surface crossings. For CNG **6**, two minima

were optimized in the  $S_1$  and  $S_2$  potentials, respectively ( $S_{1,\min}$  and  $S_{2,\min}$  see Figure 6). Interestingly, for CNG **7** and CNG **8**, see Figure 6, all the geometry optimizations either converge into two different  $S_1$  minima ( $S_{1,\min}A$  and  $S_{1,\min}B$ ), or into a single minimum in the  $S_2$  potential  $S_{2,\min}$ . It should be remarked here that the population of the  $S_{1,\min}B$  and  $S_{2,\min}$  minima is expected either from the population of electronic excited states above the  $S_1$  or upon thermal activation from  $S_{1,\min}A$ . The geometries of these minima are compared with respect to the FC structure in Figures S20–S22 (Supporting Information). Both adiabatic and vertical energies for these minima are reported in the schematic representation of the PES for CNG **6**, **7**, and **8** in Figure 6, top, middle, and bottom panel, respectively. For both subunits, **Cor** and **HBC-tBu**, a single minimum was found in the  $S_1$ ,  $S_{1,\min}$ , as reported in Figures S23 and S24 (Supporting Information). Little geometric reorganization was observed for the smaller systems as can be seen in Figures S25 and S26 (Supporting Information).

To allow for a better comparison with experimental fluorescence spectra, a vibrationally-resolved version of the calculated emission spectra is shown in Figure 7. For all three systems, the broad spectrum arising from the  $S_{1,\min}A$  virtually reproduces the shape of the experimental signal. This is consistent with the greater stability of this minimum and thus its overall population after the relaxation of the system. Moreover, the relative intensity change in the shoulders upon change in the excitation energy for the CNG **7** and **8** (Figure 1) can be attributed to the partial emission from  $S_{1,\min}B$ , which gets populated from higher-lying excited states according to our optimizations from the FC geometry (see Figure 6). In fact, the emission signal of minimum  $S_{1,\min}B$  is, for both CNGs, slightly blue shifted compared to that of minimum  $S_{1,\min}A$ , which would readily explain the experimental changes in the relative intensity of the shoulder at 493 nm in CNG **8**, upon increasing the excitation energy and thus the population of the less stable minimum. The changes in the relative intensity of the shoulder at 530 nm in CNG **7** are not so evident, although we hypothesize that the red edge vibrational broadening of the emission spectrum arising from  $S_{1,\min}B$  might contribute to the increase of the absorbance of the shoulder to the red of

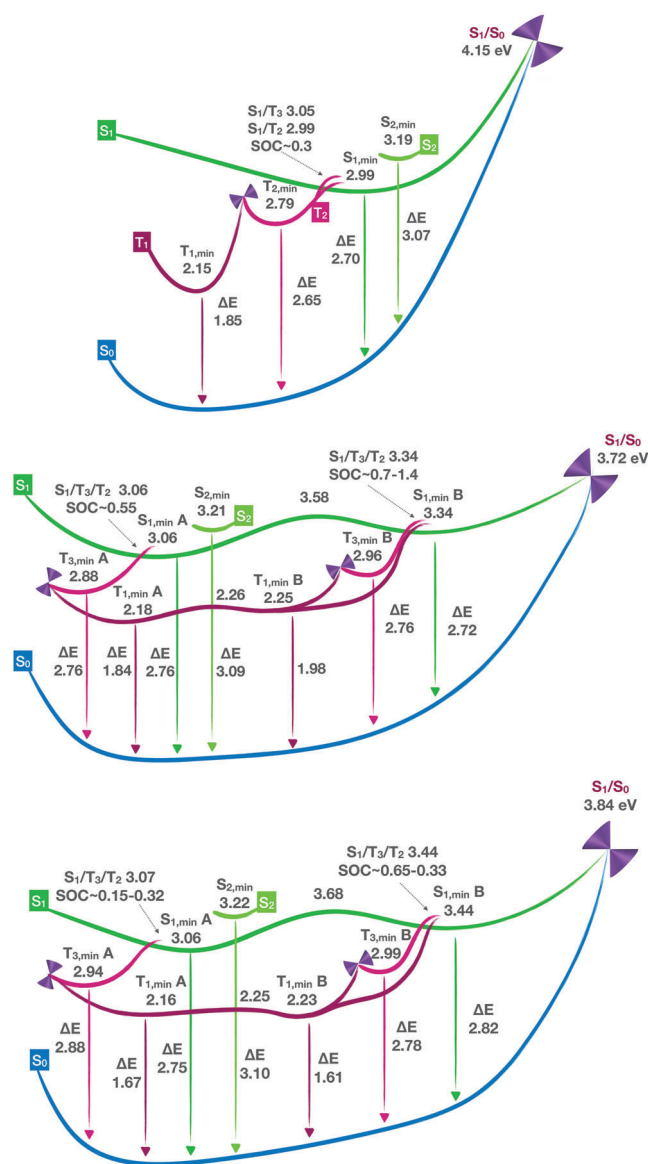


**Figure 6.** Schematic representation of the potential energy profiles for (top) CNG 6, (middle) CNG 7, and (bottom) CNG 8 along the coordinate relevant to their deactivation. Vertical and adiabatic relative energies with respect to the respective  $S_0$  minimum are given in eV. SOC matrix elements are given in  $\text{cm}^{-1}$ .

the absorption maximum with shorter wavelengths because of the population of this minimum. The B to A population transfer would also be thermally possible after surpassing an energy barrier of  $\approx 0.25$  eV, which is also consistent with the lower population of  $S_{1,\text{min}}\text{B}$  and thus its lesser contribution to the emission spectra. **Cor** and **HBC-*t*Bu** emission spectra were vibrationally-resolved for the single  $S_{1,\text{min}}$  found in their excited PES, and are shown in Figure S19 (Supporting Information) central panel. The experimental spectral shape was very well reproduced, indicating the unique participation of this minimum and discarding a more complex singlet potential energy landscape as found for CNG 6, 7, and 8.

Aiming at a more precise analysis of the excited states responsible for the emission bands, the Natural Transition Orbitals (NTOs) of the excitations contributing to a larger extent to the minima have been analyzed. The NTOs and the corresponding electron-hole plots for the minima are collected in Figures S27–S29 (Supporting Information) for CNG 6, 7, and 8 respectively. According to the NTO analysis, the  $S_{1,\text{min}}\text{A}$  and  $S_{1,\text{min}}\text{B}$  of both CNG 7 and CNG 8 show a markedly different character. In particular,  $S_{1,\text{min}}\text{A}$  is delocalized along the two subunits, while  $S_{1,\text{min}}\text{B}$  is mainly localized on the **Cor** moiety (see Figures S28 and S29, Supporting Information). Since both correspond to minima in the lowest excited potential at their respective geometry, dual emission from these minima follows the Kasha rule. For the smaller fragments, the NTOs are depicted in Figures S30 and S31 (Supporting Information).

For CNG 7, the lower-intensity emission band occurring at 400–450 nm is ascribed to a minimum in the  $S_2$ , allowing its classification as a non-Kasha chromophore. The  $S_2$  minimum arises from the same excitation in CNG 6 and 7, but differs for CNG 8, as shown in Figures S27–S29 (Supporting Information). An analysis of the vibrationally resolved fluorescence spectra simulated for the singlet minima of the three CNGs reveals the greatest shift between the  $S_{2,\text{min}}$  with respect to the  $S_1$  emission for CNG 7, which translates into two separate emission signals. However, based on the collected data, it is not possible to discard non-Kasha emission from the three CNGs, which might be masked in CNG 6 and 8 by the width of the  $S_1$  emission. Moreover, very weak fluorescence in the same region as for CNG 7 was experimentally also observed for CNG 6 (not shown here). To account for the possible population of the  $S_2$  minimum, we have resorted to a kinetic model to estimate the IC constants between  $S_{1,\text{min}}\text{A}$  and  $S_{2,\text{min}}$  in CNG 7.<sup>[25]</sup> Since IC rates are highly sensitive to the adiabatic energy difference between the pair of states involved, more reliable RI-ADC(2)/def2-SVP energies were calculated in order to obtain a more accurate energy gap between the two minima. In fact, a slightly smaller energy gap of 0.11 eV was obtained with the latter method (0.15 eV at TDDFT). According to our calculations, the ( $S_2 \rightarrow S_1$ ) IC rate is only one order of magnitude larger than the one of the reverse process ( $S_1 \rightarrow S_2$ ):  $10^{12}$  versus  $10^{11} \text{ s}^{-1}$ . A similar ratio for the IC rates between both  $S_{1,\text{min}}\text{A}$  and  $S_{2,\text{min}}$  minima was obtained for CNG 6 and 8, supporting non-Kasha emission for the three CNGs.<sup>[26]</sup> This discussion, however, does not take into account possible contributions to the high-energy PL band from singlet states lying above the  $S_2$  (see Figure 5), which could also readily explain the large energy difference (0.7 eV) between the onset of the high-energy and main PL bands of CNG 7, in terms of vertical energy differences. Nevertheless, the vibrationally resolved emission from the  $S_2$  and  $S_1$  minima seems to qualitatively account for the observed differences, which consistently with the calculated IC rates between these two states allow us to conclude that the  $S_{2,\text{min}}$  is the main responsible for the higher-energy non-Kasha PL band.

Radiative rate constants corresponding to the main fluorescence bands have been also calculated for the  $S_{1,\text{min}}\text{A}$ , which are responsible for the main fluorescence emission bands: a) CNG 6  $2.74 \times 10^8 \text{ s}^{-1}$  ( $\tau = 3.65$  ns), b) CNG 7  $2.57 \times 10^8 \text{ s}^{-1}$  ( $\tau = 3.89$  ns), c) CNG 8  $2.71 \times 10^8 \text{ s}^{-1}$  ( $\tau = 3.69$  ns), d) **Cor**  $1.84 \times 10^6 \text{ s}^{-1}$  ( $\tau = 543$  ns), and e) **HBC-*t*Bu**  $5.24 \times 10^2 \text{ s}^{-1}$  ( $\tau = 1.91$  ms). In the case of **Cor**, a fluorescence quantum yield of 0.03 and a

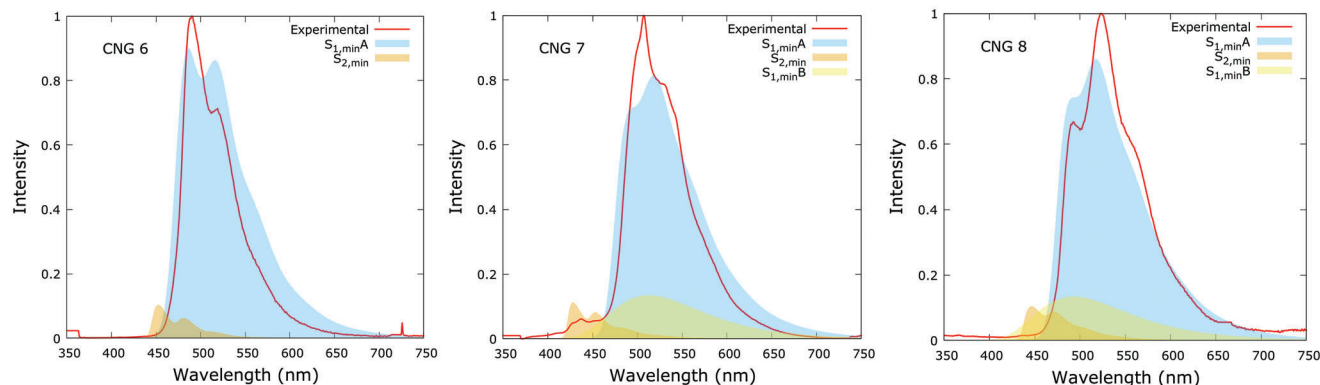


**Figure 7.** Calculated normalized vibrationally-resolved emission spectra at room temperature of CNG **6** (left), **7** (center) and **8** (right) in  $\text{CHCl}_3$  using a FWHM of 0.01 eV at the wB97X-D/def2-SVP/PCM level of theory. Spectra are redshifted by 0.35, 0.35, and 0.35 eV, respectively, to match experimental spectra.

fluorescence lifetime of 7.3 ns was reported previously at room temperature in degassed dichloromethane.<sup>[27]</sup> For **Cor** in air-saturated n-octane we measured a fluorescence quantum yield of 0.02 and a mono-exponential decay with a lifetime of 9.73 ns at room temperature. Using  $k_r = \phi_{\text{fluo}}/\tau = 2.1 \times 10^6 \text{ s}^{-1}$  good agreement with theory is obtained. Simultaneously  $k_{\text{nr}} + k_{\text{ISC}} = k - k_r = \tau^{-1} - k_r = 1.01 \times 10^8 \text{ s}^{-1}$  is obtained from those values. In fact, for **Cor** the  $S_0 \leftarrow S_1$  transition is electric-dipole forbidden and its electronic origin can be expected at  $\approx 380 \text{ nm}$ ,<sup>[28]</sup> consistent with our observations. A similar situation exists for non-functionalized **HBC**,<sup>[29]</sup> where a forbidden electronic origin at 428 nm was reported, again in agreement with the calculations and with spectra shown in Figure S7 (Supporting Information). It should be remarked here that the butyl groups of **HBC-tBu** are expected to have only a minor influence on those findings.

To map the complete relaxation mechanism to the ground states of these systems and to provide a molecular rationalization of the photophysical properties of these systems we have located  $S_1/S_0$  IC funnels, see Figure 6. The access to these funnels entails, in all the systems considered, a significant distortion of the structures (as seen in Figures S20–S22, Supporting Information) that translate into non-negligible energy gaps with the most stable  $S_1$  minima, amounting to 0.66 eV (CNG **7**) < 0.78 eV (CNG **8**) < 1.16 eV (CNG **6**). For CNG **7** and **8**, the leading coordinate responsible for the access to  $S_1/S_0$  CI corresponds to the out-of-plane movement of the Cl atom (CNG **7**) and H atom (CNG **8**) sitting at the same position, while for CNG **6**, IC to  $S_0$  requires planarization of the **HBC-tBu** moiety and a decrease of the dihedral angle described by the two subunits. Furthermore, for CNG **7** and CNG **8** deactivation from the most stable minima implies overcoming a preceding energy barrier to access the secondary  $S_{1,\text{min}}\text{B}$ : ( $S_{1,\text{min}}\text{A} \rightarrow S_{1,\text{min}}\text{B}$ ) and ( $S_{1,\text{min}}\text{B} \rightarrow S_1/S_0$ ). The blocking of the IC routes by relatively high energy barriers in the excited state potential energy profiles opens the door to alternative relaxation mechanisms, different from the IC and singlet radiative emission, including the deactivation of the systems along the triplet manifold. In the case of **Cor**, a small value of  $k_{\text{nr}}$  results, if it is assumed that  $k_{\text{ISC}}$  dominates the total decay rate of  $S_1$ . In fact, a high intersystem crossing yield and intersystem crossing rate of  $\phi_{\text{ISC}} = 0.89$ ,  $k_{\text{ISC}} = 5 \times 10^7 \text{ s}^{-1}$ , a low IC yield and non-radiative relaxation rate of  $\phi_{\text{IC}} = 0.09$ ,  $k_{\text{nr}} = 5 \times 10^6 \text{ s}^{-1}$ , a radiative rate of

$k_r = 1.4 \times 10^6 \text{ s}^{-1}$  and a simultaneously low fluorescence quantum yield  $\phi_{\text{fluo}} = 0.02$  have been reported before for **Cor** in degassed cyclohexane at room temperature, based on photoacoustic experiments.<sup>[30]</sup> All these parameters are very much in line with the discussion of the quantum-chemical calculations provided above. The high values of  $\phi_{\text{ISC}}$  and  $k_{\text{ISC}}$  for **Cor** are indeed unsurprising as it is known<sup>[31]</sup> that curvature and twist favor intersystem crossing. Indeed, high intersystem crossing rates have also been reported for other curved nanographenes: single wall carbon nanotubes:<sup>[32]</sup>  $5 \times 10^{10} \text{ s}^{-1}$ ,  $\text{C}_{60}$  fullerene:<sup>[33]</sup>  $\approx 7 \times 10^8 \text{ s}^{-1}$  and carbon nanohorns:<sup>[34]</sup>  $7.2 \times 10^8 \text{ s}^{-1}$ .

Comparing the radiative rates and the fluorescence quantum efficiencies for **Cor** with the experimental values for the CNGs listed in Table 2 it is immediately clear that both are more than an order of magnitude higher for the CNGs than for **Cor**. This is of course due to the coupling between the **Cor** and **HBC-tBu** fragments and the corresponding extension of their electronic wave functions and the reduction in the symmetries of the latter. Using the same kinetic models, the IC deactivation rates were computed for the three systems: a) CNG **6**  $2.92 \times 10^7 \text{ s}^{-1}$ , b) CNG **7**  $2.59 \times 10^8 \text{ s}^{-1}$ , and c) CNG **8**  $2.64 \times 10^8 \text{ s}^{-1}$ . While for **Cor** an  $S_1/S_0$  IC funnel was found at a high energy of 1.15 eV above the  $S_{1,\text{min}}$ , for **HBC-tBu** the  $S_1/S_0$  IC optimization was difficult to converge and a crossing was found at an unphysically high value of 10 eV above the  $S_{1,\text{min}}$ . In any case, it is reasonable to expect weak direct IC to the ground state for both systems, considering the great geometric reorganization necessary to reach the IC, which indicates the rigidity of both systems (see Figures S25 and S26, Supporting Information). Comparing again with the experimental values of Table 2 we find  $k_{\text{nr}} + k_{\text{ISC}} = 4.5 \times 10^7 \text{ s}^{-1}$ ,  $6.8 \times 10^7 \text{ s}^{-1}$ ,  $1.4 \times 10^8 \text{ s}^{-1}$  for **6**, **7**, and **8**, respectively, values which, however, following the discussion above, should contain a significant contribution from  $k_{\text{ISC}}$ . The experimental results shown in Figure S5b (Supporting Information), i.e., the somewhat longer decay times of CNG **7** for the high energy fluorescence band, tentatively ascribed above to emission from  $S_2$ , relative to those of the main fluorescence band, can now be rationalized using two arguments: i) the intersystem crossing rate for  $S_2$  might be smaller than  $k_{\text{ISC}}$  for  $S_1$  and ii) the radiative rate for transitions from  $S_2$  may be smaller than  $k_r$  of  $S_1$ . The latter argument is supported in fact by our quantum-chemical calculations that result in  $k_r = 3.3 \times 10^7 \text{ s}^{-1}$  ( $f = 0.084$ )



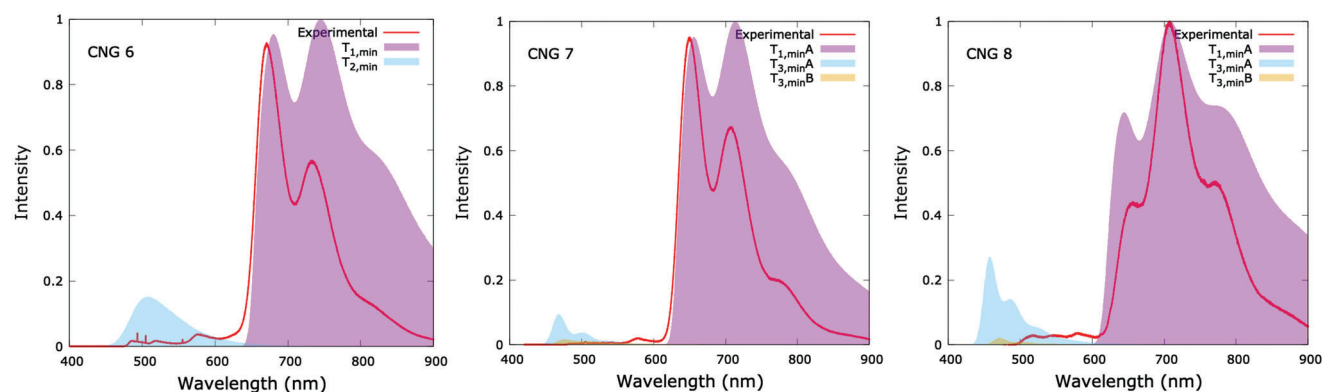


**Figure 8.** Calculated normalized vibrationally resolved phosphorescence emission spectra using a FWHM of 0.01 eV at 65 K of CNGs **6** (left), **7** (center) and **8** (right) in  $\text{CHCl}_3$  at the wB97X-D/def2-SVP/PCM level of theory. Spectra are redshifted by 0.2, 0.1, and 0.2 eV respectively, to match experimental spectra.

and  $k_r = 2.6 \times 10^8 \text{ s}^{-1}$  ( $f = 0.86$ ) for the vertical transitions to the ground state from  $S_2$  and  $S_1$ , respectively.

### 2.2.3. Triplet Potential Energy Surfaces and Phosphorescence

To complete the photophysical picture, we also explored the potential routes for ISC. Near each of the  $S_{1,\text{min}}$  geometries, both the  $T_2$  and  $T_3$  turn out to be very close to the first singlet state. The excited state energies and calculated SOC are presented in Figure 6. It is obvious that the calculated  $T_2/T_3-T_1$  energy gaps are significantly larger than the experimental values listed in Table 4. Despite this quantitative disagreement, possibly due to not accounting for the vibronic effects and also to the uncertainty of the experimentally determined onsets of the apparently thermally activated delayed emission bands, the mere existence of higher energy triplet minima ( $T_{3,\text{min}}$  or  $T_{2,\text{min}}$ ), relatively close to  $T_1$ , for all CNG can explain the splitting reported in Table 4 and corresponding to Figure S8 (Supporting Information).

As expected from the electronic structure of the systems and the nature of their electronic excited states, the SOC values at these geometries range from 0.3 to 1.4  $\text{cm}^{-1}$ . Relaxation of the populated triplet states, either  $T_3$  or  $T_2$ , in CNG **6** would populate a  $T_{2,\text{min}}$ , which would further relax to a  $T_{1,\text{min}}$  through a  $T_2/T_1$  IC funnel lying slightly above the minimum ( $\approx 0.2$  eV). For CNG **7** and **8**, ISC at the vicinity of both,  $S_{1,\text{min}}$ A and  $S_{1,\text{min}}$ B provides access to two  $T_3$  minima,  $T_{3,\text{min}}$ A and  $T_{3,\text{min}}$ B, respectively, that would retain a fraction of the excited state population. The occurrence of close lying IC funnels to the  $T_3$  minima positions would ultimately drive the bulk of the excited population towards the global  $T_{1,\text{min}}$ A and the local  $T_{1,\text{min}}$ B. The transfer of population from  $T_{1,\text{min}}$ B to  $T_{1,\text{min}}$ A would occur through a small energy barrier of  $\approx 0.02$  eV. For CNG **7** and **8**, there is a correspondence between  $S_{1,\text{min}}$ A and  $T_{1,\text{min}}$ A, and between  $S_{1,\text{min}}$ B and  $T_{1,\text{min}}$ B characters, which is in line with their structural analogy. Thus, while the “A” minima show a delocalized excitation along the two moieties, the “B” minima are localized on the **Cor** fragment, as detailed above for their singlet analogues. Obviously, the calculated  $T_1-T_n$  splittings for  $n = 2, 3$  are much larger than those listed in Table 4, which were based on the tentative assignment of weak emission bands in Figure S8 (Supporting Information), marked by arrows.

This might be caused by significantly higher onsets of this emission band being covered by TADF and background signals.

**Cor** exhibits a virtual  $S_1-T_3$  degeneracy at the  $S_{1,\text{min}}$  geometry, with a SOC value of the same order of magnitude as those obtained for the CNG derivatives ( $\approx 0.6 \text{ cm}^{-1}$ ). In contrast, **HBC-tBu** exhibits degeneracy of  $S_1$  with a higher lying triplet state ( $T_6$ ), but the SOC value is significantly lower ( $\approx 0.0005 \text{ cm}^{-1}$ ). In both cases, a single  $T_{1,\text{min}}$  was found, that would be reached after successive IC along the triplet manifold. **Cor** population of  $T_{1,\text{min}}$  proceeds via a shallow  $T_{3,\text{min}}$  (see Figure S23, Supporting Information). Interestingly, the moderate SOC values for the three CNGs and **Cor** could satisfactorily explain the reverse ISC leading to TADF, which, on the other hand, was not found experimentally for the **HBC-tBu**, consistent with extremely low SOC found for this fragment.

The simulated vibrationally-resolved phosphorescence spectra are shown in Figure 8. For the three CNGs,  $T_{1,\text{min}}$ (A) was accounted for since, according to the topography of the triplet PES, this should be the predominantly populated minimum. The comparison of the simulated and experimental spectra in the low energy range reveals an excellent agreement, the computed spectra being able to reproduce the position of the emission and to qualitatively delineate the relative contribution of the different vibrational states to the emission band. Despite the majority contribution of the  $T_{1,\text{min}}$ (A) to the phosphorescence spectra of CNGs **7** and **8**, residual contributions from other triplet minima cannot be completely discarded, such as  $T_{3,\text{min}}$ A and  $T_{3,\text{min}}$ B that were also included in Figure 8 to account for the high-energy phosphorescence, clearly observed in Figure S7 (Supporting Information). Meanwhile, for CNG **6**, both  $T_{2,\text{min}}$  and  $T_{1,\text{min}}$  were considered, showing again a very reasonable agreement with experiment. Nevertheless, emission from the higher-lying triplet minima appears blue-shifted in the calculated spectra. The calculated radiative rate constants for the  $T_{1,\text{min}}$ (A), which are responsible for the main phosphorescence emission bands, are: a) CNG **6**  $1.12 \times 10^{-2} \text{ s}^{-1}$  ( $\tau = 9 \times 10^3 \text{ s}$ ), b) CNG **7**  $3.53 \times 10^{-1} \text{ s}^{-1}$  ( $\tau = 3 \times 10^2 \text{ s}$ ), and c) CNG **8**  $3.61 \times 10^{-1} \text{ s}^{-1}$  ( $\tau = 3 \times 10^2 \text{ s}$ ). This must be compared with the experimental values obtained at 65 K, which are in the range of seconds (compare Figure 2 and Table 3). The vibrationally-resolved phosphorescence spectra for **Cor** and **HBC-tBu** from  $T_{1,\text{min}}$  is shown in Figure S19

(Supporting Information) right panel. The experimental spectral shape is closely reproduced by our simulations, indicating the unique participation of this minimum, whose state character is depicted in Figures S29 and S30 (Supporting Information). In this case, the calculated radiative rate constants for the  $T_{1,\min}$ , which are responsible for the main phosphorescence emission bands, are: d) **Cor**  $4.22 \times 10^{-2} \text{ s}^{-1}$  ( $\tau = 2.37 \times 10^1 \text{ s}$ ), and e) **HBC-tBu**  $4.83 \times 10^{-1} \text{ s}^{-1}$  ( $\tau = 2 \times 10^0 \text{ s}$ ), values that are closer to the experimental phosphorescence lifetimes reported in Table 3 than for the CNGs.

### 3. Conclusion

Multiple emissions have been identified experimentally for the CNGs investigated: dual fluorescence in the case of **7** and **8**, arising, according to the TD-DFT calculations, from double well  $S_1$  potential; dual phosphorescence that can be rationalized by the calculations as emission from two  $T_1$  minima, one of them dominating the phosphorescence; hot (non-Kasha) fluorescence in the case of **7**, tentatively ascribed to emission from  $S_2$  and weak hot phosphorescence tentatively ascribed to emission from  $T_2$  for **6** and  $T_3$  for **7** and **8**; in addition, TADF has been found in a limited temperature range determined on the one hand by the thermal energy necessary for thermal activation of the singlet from a triplet  $T_n$  state and, on the other hand, by the non-radiative decay of the triplet states, which, in the case of  $T_1$ , appears to follow an Arrhenius behavior. The activation energies corresponding to those Arrhenius laws are found to be in the range 77–175 meV and may be ascribable to thermal activation of molecular vibrations coupling to  $T_1$ . This aspect, however, was not further investigated in the present work. Interestingly, non-radiative decay of  $T_1$ , measured by a rate  $k_{nr,T}$ , has usually been neglected in the study of TADF materials, even though the applications of such materials require their use at room temperature. This is mainly due to the usually unknown value of  $k_{nr,T}$ . In addition, in temperature-dependent studies of TADF materials the difficulty of analytic modeling of the non-radiative processes involving  $T_1$  has frequently led to neglect of them completely.

As the  $S_1$ – $T_1$  splitting are too large for direct thermal activation of  $S_1$  from  $T_1$  in this temperature range, TADF must proceed from populations trapped in higher  $T_n$  states after pulsed excitation. According to the TD-DFT calculations, those states could be  $T_{2\min}$  in the case of **6** and  $T_{3\min}$  in the case of **7** and **8**, recall Figure 6. The  $T_2/T_3$ – $T_1$  barrier heights predicted by TD-DFT, however, appear to be too small to produce a sufficient retardation of non-radiative relaxation of the  $T_2/T_3$  electronic states towards  $T_1$ , which would be necessary to explain the experimental findings. This may be ascribed to error inherent to the level of theory employed. On the other hand, TD-DFT describes very well the absorption, fluorescence, and phosphorescence spectra.

To conclude, the insights obtained from the spectroscopy of these chiral and non-chiral novel molecular nanographene architectures might pave the way for a new series of non-metal, non D/A-type molecules exhibiting TADF at room temperature, displaying relatively narrow-band fluorescence, phosphorescence, as well as TADF emission via hRISC from higher triplet excited states.

### Supporting Information

Supporting Information is available from the Wiley Online Library or from the author.

### Acknowledgements

J.M. F.-G., D.G.-F. and N.M. acknowledge financial support from the Spanish MICINN (Project PID2020-114653RB-I00), they also acknowledge financial support from the ERC (SyG TOMATTO ERC-2020-951224) and from the "MAD2D-CM)-UCM" project funded by Comunidad de Madrid, by the Recovery, Transformation and Resilience Plan, and by NextGenerationEU from the European Union. F. R.-G. acknowledges the support of a fellowship from "la Caixa" Foundation (LCF/BQ/DR19/11740024, Grant No. ID 100010434). I.C. and F.R.-G. also thankfully acknowledge financial support from the PID2021-125207NB-C31 project of the Ministerio de Ciencia e Innovación of Spain. I.C. thanks the Ramón y Cajal Program (Grant RyC-2016-20489). L.M.F. thanks the Madrid Government (Comunidad de Madrid-Spain) under the Multiannual Agreement with Universidad Autónoma de Madrid in the line Support to Young Researchers, in the context of the V PRICIT (Regional Programme of Research and Technological Innovation) (SI3/PJ1/2021-00331). S. F. acknowledges funding from the Chinese Scholarship Council (grant no. 202008330343). The authors were also grateful for the generous allocation of computer time and continued technical support by the Centro de Computación Científica of the UAM (CCC-UAM). The authors thank Javier Cerezo for the useful hints in the use of FCClasses. R.W. acknowledges funding from MCIN/AIE and the European Union through projects RTI2018-097508-B-I00 and PID2019-107808RA-I00 and from the Comunidad de Madrid and the European Union structural funds through grants S2018/NMT-4511 and PEJD-2017-PRE/IND-4862. IMDEA Nanociencia acknowledges support from the "Severo Ochoa" Programme for Centers of Excellence in R&D (MICIN, CEX2020-001039-S).

### Conflict of Interest

The authors declare no conflict of interest.

### Author Contributions

S.R.-B. and F.R.-G. contributed equally to this work. J.M.F.-G. and N.M. synthesized, purified and structurally characterized the materials investigated. S.R.B. and R.W. performed the experimental part of the study, S.F. participated in the experimental investigation of the Cor and HBC-tBu fragments; F.R.-G., L.M.-F., and I.C. performed the quantum-chemical calculations; S.B. and D.G.-F. performed additional experimental work on double check samples; S.R.-B., D.G.-F., I.C., N.M., and R.W. participated in writing the manuscript.

### Data Availability Statement

The data that support the findings of this study are available from the corresponding author upon reasonable request.

### Keywords

curved nanographenes, multiple emission, phosphorescence, thermally activated delayed fluorescence (TADF)

Received: December 23, 2022  
Revised: March 31, 2023  
Published online: June 18, 2023

- [1] a) Y. Gu, Z. Qiu, K. Müllen, *J. Am. Chem. Soc.* **2022**, *144*, 11499; b) A. Borissov, Y. K. Maurya, L. Moshniha, W. S. Wong, M. Żyła-Karwowska, M. Stępień, *Chem. Rev.* **2022**, *122*, 565; c) Z. Liu, S. Fu, X. Liu, A. Narita, P. Samorì, M. Bonn, H. I. Wang, *Adv. Sci.* **2022**, *9*, 2106055; d) R. S. Jassas, E. U. Mughal, A. Sadiq, R. I. Alsantali, M. M. Al-Rooqi, N. Naeem, Z. Moussa, S. A. Ahmed, *RSC Adv.* **2021**, *11*, 32158; e) S. M. Suresh, D. Hall, D. Beljonne, Y. Olivier, E. Zysman-Colman, *Adv. Funct. Mater.* **2020**, *30*, 1908677; f) X. Y. Wang, X. Yao, A. Narita, K. Müllen, *Acc. Chem. Res.* **2019**, *52*, 2491; g) I. Pozo, E. Guistián, D. Pérez, D. Peña, *Acc. Chem. Res.* **2019**, *52*, 2472; h) M. Grzybowski, B. Sadowski, H. Butenschön, D. T. Gryko, *Angew. Chem., Int. Ed.* **2020**, *59*, 2998; i) M. Stępień, E. Gonka, M. Żyła, N. Sprutta, *Chem. Rev.* **2017**, *117*, 3479; j) H. Ito, K. Ozaki, K. Itami, *Angew. Chem., Int. Ed.* **2017**, *56*, 11144; k) *Polyarenes I. Topics in Current Chemistry*, (Eds.: J. Siegel, Y. T. Wu), Springer, Berlin/Heidelberg, Germany **2014**, Vol. 349; l) C. Zhang, Y. Liu, X. Q. Xiong, L. H. Peng, L. Gan, C. F. Chen, H. B. Xu, *Org. Lett.* **2012**, *14*, 5912; m) K. Müllen, J. P. Rabe, *Acc. Chem. Res.* **2008**, *41*, 511.
- [2] a) R. Sekiya, T. Haino, *Chem. - Eur. J.* **2021**, *27*, 187; b) B. P. Mathew, M. R. Kuram, *Inorg. Chim. Acta* **2019**, *490*, 112.
- [3] a) Y. Fei, J. Liu, *Adv. Sci.* **2022**, *9*, 2201000; b) K. Kato, K. Takaba, S. Maki-Yonekura, N. Mitoma, Y. Nakanishi, T. Nishihara, T. Hatakeyama, T. Kawada, Y. Hijikata, J. Pirillo, L. T. Scott, K. Yonekura, Y. Segawa, K. Itami, *J. Am. Chem. Soc.* **2021**, *143*, 5465; c) E. M. Muza-mmil, D. Halilovic, M. C. Stuparu, *Commun. Chem.* **2019**, *2*, 58; d) I. R. Márquez, S. Castro-Fernández, A. Millán, A. G. Campaña, *Chem. Commun.* **2018**, *54*, 6705; e) P. J. Evans, J. Ouyang, L. Favereau, J. Crassous, I. Fernández, J. Perles, N. Martín, *Angew. Chem., Int. Ed.* **2018**, *57*, 6774; f) E. M. Pérez, N. Martín, *Chem. Soc. Rev.* **2015**, *44*, 6425.
- [4] a) S. K. Behera, S. Y. Park, J. Gierschner, *Angew. Chem., Int. Ed.* **2021**, *60*, 22624; b) J. M. Teng, Y. F. Wang, C. F. Chen, *J. Mater. Chem. C* **2020**, *8*, 11340; c) F. M. Xie, J. X. Zhou, Y. Q. Li, J. X. Tang, *J. Mater. Chem. C* **2020**, *8*, 9476; d) Z. Yang, Z. Mao, Z. Xie, Y. Zhang, S. Liu, J. Zhao, J. Xu, Z. Chi, M. P. Aldred, *Chem. Soc. Rev.* **2017**, *46*, 915; e) L. Bergmann, D. M. Zink, S. Bräse, J. Baumann, D. Volz, *Top. Curr. Chem.* **2016**, *374*, 22; f) S. Mukherjee, P. Thilagar, *Chem. Commun.* **2015**, *51*, 10988; g) Z. Chi, X. Zhang, B. Xu, X. Zhou, C. Ma, Y. Zhang, S. Liu, J. Xu, *Chem. Soc. Rev.* **2012**, *41*, 3878.
- [5] a) S. Zank, J. M. Fernández-García, A. J. Stasyuk, A. A. Voityuk, M. Krug, M. Solà, D. M. Guldí, N. Martín, *Angew. Chem., Int. Ed.* **2022**, *61*, e202112834; b) J. I. Urgel, M. Di Giovannantonio, Y. Segawa, P. Ruffieux, L. T. Scott, C. A. Pignedoli, K. Itami, R. Fasel, *J. Am. Chem. Soc.* **2019**, *141*, 13158; c) Q. Huang, G. Zhuang, H. Jia, M. Qian, S. Cui, S. Yang, P. Du, *Angew. Chem., Int. Ed.* **2019**, *58*, 6244; d) H. A. Lin, Y. Sato, Y. Segawa, T. Nishihara, N. Sugimoto, L. T. Scott, T. Higashiyama, K. Itami, *Angew. Chem., Int. Ed.* **2018**, *57*, 2874; e) Y. Dai, Z. Li, J. Yang, *Carbon* **2016**, *100*, 428.
- [6] a) Q. Dang, Y. Jiang, J. Wang, J. Wang, Q. Zhang, M. Zhang, S. Luo, Y. Xie, K. Pu, Q. Li, Z. Li, *Adv. Mater.* **2020**, *32*, 2006752; b) X. Huang, J. Song, B. C. Yung, X. Huang, Y. Xiong, X. Chen, *Chem. Soc. Rev.* **2018**, *47*, 2873; c) S. Xu, C. Z. R. Chen, W. Huang, *Adv. Mater.* **2016**, *45*, 2707; d) M. A. Haidekker, E. A. Theodorakis, *J. Mater. Chem.* **2016**, *4*, 2707; e) J. Zhang, Q. Zou, H. Tian, *Adv. Mater.* **2013**, *3*, 378.
- [7] X. Wu, J. W. Huang, B. K. Su, S. Wang, L. Yuan, W. Q. Zheng, H. Zhang, Y. X. Zheng, W. Zhu, P. T. Chou, *Adv. Mater.* **2022**, *34*, 2105080.
- [8] M. A. El-Sayed, *J. Chem. Phys.* **1963**, *38*, 2834.
- [9] M. Alías Rodríguez, C. de Graaf, M. Huix-Rotllant, *J. Am. Chem. Soc.* **2021**, *143*, 21474.
- [10] a) Y. Dong, A. A. Sukhanov, J. Zhao, A. Elmali, X. Li, B. Dick, A. Karatay, V. K. Voronkova, *J. Phys. Chem. C* **2019**, *123*, 22793; b) V. K. Singh, C. Yu, S. Badgujar, Y. Kim, Y. Kwon, D. Kim, J. Lee, T. Akhter, G. Thangavel, L. S. Park, J. Lee, P. C. Nandajan, R. Wannemacher, B. Milián-Medina, L. Luer, K. S. Kim, J. Gierschner, M. S. Kwon, *Nat. Catal.* **2018**, *1*, 794.
- [11] a) Q. Liao, Q. Li, Z. Li, *ChemPhotoChem* **2021**, *5*, 694; b) K. Schmidt, S. Brovelli, V. Coropceanu, D. Beljonne, J. Cornil, C. Bazzini, T. Caronna, R. Tubino, F. Meinardi, Z. Shuai, J. L. Brédas, *J. Phys. Chem. A* **2007**, *42*, 10490.
- [12] a) X. Wang, Y. Sun, G. Wang, J. Li, X. Li, K. Zhang, *Angew. Chem., Int. Ed.* **2021**, *60*, 17138; b) K. Narushima, Y. Kiyota, T. Mori, S. Hirata, M. Vacha, *Adv. Mater.* **2019**, *10*, 1807268; c) D. Li, F. Lu, J. Wang, W. Hu, X. M. Cao, X. Ma, Tian, *J. Am. Chem. Soc.* **2018**, *140*, 1916; d) T. Ogoshi, H. Tsuchida, T. Kakuta, T. A. Yamagishi, A. Taema, T. Ono, M. Sugimoto, M. Mizuno, *Adv. Funct. Mater.* **2018**, *28*, 1707369; e) S. Cai, H. Shi, J. Li, L. Gu, Y. Ni, Z. Cheng, S. Wang, W. W. Xiong, L. Li, Z. An, W. Huang, *Adv. Mater.* **2017**, *29*, 1701244; f) S. Hirata, K. Totani, J. Zhang, T. Yamashita, H. Kaji, S. R. Marder, T. Watanabe, C. Adachi, *Adv. Funct. Mater.* **2013**, *23*, 3386; g) Z. An, C. Zheng, Y. Tao, R. Chen, H. Shi, T. Chen, Z. Wang, H. Li, R. Deng, X. Liu, W. Huang, *Nat. Mater.* **2015**, *14*, 685.
- [13] a) H. Liu, Z. Liu, G. Li, H. Huang, C. Zhou, Z. Wang, C. Yang, *Angew. Chem., Int. Ed.* **2021**, *60*, 12376; b) P. Rajamalli, F. Rizzi, W. Li, M. A. Jinks, A. K. Gupta, B. A. Laidlaw, I. D. W. Samuel, T. J. Penfold, S. M. Goldup, E. Zysman-Colman, *Angew. Chem., Int. Ed.* **2021**, *60*, 12066; c) L. Frédéric, A. Desmarchelier, L. Favereau, G. Pieters, *Adv. Funct. Mater.* **2021**, *31*, 2010281; d) R. Ansari, W. Shao, S. J. Yoon, J. Kim, J. Kieffer, *ACS Appl. Mater. Interfaces* **2021**, *13*, 28529; e) G. Dai, M. Zhang, K. Wang, X. Fan, Y. Shi, D. Sun, W. Liu, J. Chen, J. Yu, X. Ou, S. Xiong, C. Zheng, X. Zhang, *ACS Appl. Mater. Interfaces* **2021**, *13*, 25193; f) F. Fang, L. Zhu, M. Li, Y. Song, M. Sun, D. Zhao, J. Zhang, *Adv. Sci.* **2021**, *24*, 2102970; g) H. Abroshan, Y. Zhang, X. Zhang, C. Fuentes-Hernandez, S. Barlow, V. Coropceanu, S. R. Marder, B. Kippelen, J. L. Brédas, *Adv. Funct. Mater.* **2020**, *30*, 2005898; h) M. Hasan, A. Shukla, V. Ahmad, J. Sobus, F. Bencheikh, S. K. M. McGregor, M. Mamada, C. Adachi, S. C. Lo, E. B. Namdas, *Adv. Funct. Mater.* **2020**, *30*, 2000580; i) J. Liu, Z. Li, T. Hu, X. Wei, R. Wang, X. Hu, Y. Liu, Y. Yi, Y. Yamada-Takamura, Y. Wang, P. Wang, *Adv. Optical Mater.* **2019**, *7*, 1801190; j) Y. Liu, C. Li, Z. Ren, S. Yan, M. R. Bryce, *Nat. Rev. Mater.* **2018**, *3*, 18020; k) M. Y. Wong, E. Zysman-Colman, *Adv. Mater.* **2017**, *29*, 1605444.
- [14] a) H. Lim, S. J. Woo, Y. H. Ha, Y. H. Kim, J. J. Kim, *Adv. Mater.* **2022**, *34*, 2100161; b) X. Cai, Z. Qiao, M. Li, X. Wu, Y. He, X. Jiang, Y. Cao, S. J. Su, *Angew. Chem., Int. Ed.* **2019**, *58*, 13522; c) Y. Song, Y. Kim, Y. Noh, V. K. Singh, S. K. Behera, A. Abudulimu, K. Chung, R. Wannemacher, J. Gierschner, L. Luer, M. S. Kwon, *Macromolecules* **2019**, *52*, 5538.
- [15] L. Zhou, G. Xie, F. Ni, C. Yang, *Appl. Phys. Lett.* **2020**, *117*, 130502.
- [16] Y. Xu, Q. Wang, X. Cai, C. Li, Y. Wang, *Adv. Mater.* **2021**, *33*, 2100652.
- [17] J. M. Fernández-García, P. J. Evans, S. R. Medina, I. Fernández, D. García-Fresnadillo, J. Perles, J. Casado, N. Martín, *J. Am. Chem. Soc.* **2018**, *140*, 17188.
- [18] J. M. Fernández-García, P. J. Evans, S. Filippone, M. A. Herranz, N. Martín, *Acc. Chem. Res.* **2019**, *52*, 1565.
- [19] J. Mack, P. Vogel, D. Jones, N. Kavala, A. Sutton, *Org. Biomol. Chem.* **2007**, *5*, 2448.
- [20] D. Langerich, J. F. Hitznerberger, M. Marcia, F. Hampel, T. Drewello, N. Jux, *Angew. Chem., Int. Ed.* **2014**, *53*, 12231.
- [21] M. Juricek, N. L. Strutt, J. C. Barnes, A. M. Butterfield, E. J. Dale, K. K. Baldrige, J. F. Stoddart, J. S. Siegel, *Nat. Chem.* **2014**, *6*, 222.
- [22] Y. Kwon, J. Lee, Y. Noh, D. Kim, Y. Lee, C. Yu, J. C. Roldao, S. Feng, J. Gierschner, R. Wannemacher, M. S. Kwon, *Nat. Commun.* **2023**, *14*, 92.
- [23] E. Fišerová, M. Kubala, *J. Lumin.* **2012**, *132*, 2059.
- [24] a) D. García-Fresnadillo, S. Lacombe, in *Singlet Oxygen. Applications in Biosciences and Nanosciences*, (Eds. S. Nonell, C. Flors), Royal Society of Chemistry, Cambridge, UK **2016**, *1*, pp. 105–143; b) C. Schweitzer, R. Schmidt, *Chem. Rev.* **2003**, *103*, 1685; c) F. Wilkinson, W. P. Helman, A. B. Ross, *J. Phys. Chem. Ref. Data*

- 1993, 22, 113; d) A. J. McLean, D. J. McGarvey, T. G. Truscott, C. R. Lambert, E. J. Land, *J. Chem. Soc. Faraday Trans.* **1990**, 86, 3075.
- [25] J. Cerezo, F. Santoro, *J. Comput. Chem.* **2022**, 44, 626.
- [26] K. Veys, D. Escudero, *Acc. Chem. Res.* **2022**, 55, 2698.
- [27] Y.-T. Wu, D. Bandera, R. Maag, A. Linden, K. K. Baldrige, J. S. Siegel, *J. Am. Chem. Soc.* **2008**, 130, 10729.
- [28] A. Kanaoka, H. Tohyama, S. Kunishige, T. Katori, A. Nishiyama, M. Misono, N. Nakayama, H. Sakurai, M. Tsuge, M. Baba, *J. Chem. Phys.* **2019**, 151, 234305.
- [29] a) M. Kastler, J. Schmidt, W. Pisula, D. Sebastiani, K. Müllen, *J. Am. Chem. Soc.* **2006**, 128, 9526; b) Y. Hu, D. Wang, M. Baumgarten, D. Schollmeyer, K. Müllen, A. Narita, *Chem. Commun.* **2018**, 54, 13575. c) R. Yamaguchi, S. Ito, B. S. Lee, S. Hiroto, D. Kim, H. Shinokubo, *Chem Asian J* **2013**, 8, 178.
- [30] M. Yamaji, K. Takehira, T. Mikoshiba, S. Tojo, Y. Okada, M. Fujitsuka, T. Majima, S. Tobita, J. Nishimura, *Chem. Phys. Lett.* **2006**, 425, 53.
- [31] a) K. Nagarajan, A. R. Mallia, K. Muraleedharan, M. Hariharan, *Chem. Sci.* **2017**, 8, 1776; b) K. Schmidt, S. Brovelli, V. Coropceanu, D. Beljonne, J. Cornil, C. Bazzini, T. Caronna, R. Tubino, F. Meinardi, Z. Shuai, J.-L. Brédas, *J. Phys. Chem. A* **2007**, 111, 10490; c) P. Baronas, R. Komskis, E. Tankeleviciute, P. Adomenas, O. Adomeniene, S. Jurseinas, *J. Phys. Chem. Lett.* **2021**, 12, 6827.
- [32] a) J. Park, P. Deria, M. J. Therien, *J. Am. Chem. Soc.* **2011**, 133, 17156; b) F. Habenicht, O. V. Prezhdo, *J. Am. Chem. Soc.* **2012**, 134, 15648.
- [33] a) Y. Kawashima, K. Ohkubo, S. Fukuzumi, *J. Phys. Chem. A* **2012**, 116, 8942; b) A. Sastre-Santos, C. Parejo-Parados, L. Martín-Gomis, K. Ohkubo, F. Fernández-Lázaro, S. Fukuzumi, *J. Mater. Chem.* **2011**, 21, 1509.
- [34] M. Lee, O.-K. Song, J.-C. Seo, D. Kim, Y. D. Suh, S. M. Jin, S. K. Kim, *Chem. Phys. Lett.* **1992**, 196, 325.